

Improved double-phase-field algorithm based on scaled boundary finite element method for rock-like materials

Yue Zhuo, Degao Zou, Kai Chen^{*}, Yongqian Qu, Guoyang Yi, Shanlin Tian

The State Key Laboratory of Coastal and Offshore Engineering, Dalian University of Technology, Dalian, Liaoning 116024, China
School of Infrastructure Engineering, Dalian University of Technology, Dalian, Liaoning 116024, China

ARTICLE INFO

Keywords:

SBFEM
Cross-scale
Fracture analysis
Phase-field method
Polygonal element

ABSTRACT

The study of cracking analysis algorithms for rock-like materials is an important branch in the development of solid mechanics, and the related results have received extensive attention from researchers around the world. To broaden the generalizability of the phase-field method, an improved double-phase-field (DPF) algorithm based on the Scaled Boundary Finite Element Method (SBFEM) is presented. Firstly, the main governing equations are deduced and interpreted based on the nonlinear SBFEM framework. Secondly, the flexible polygon class library, data structure and solving framework for DPFM are designed by object-oriented programming. Subsequently, the presented algorithm is integrated in the self-developed finite element software GEODYNA. Thirdly, the precision is demonstrated by three classic examples, and its efficiency and practicality for complex mixed-mode fractures are validated with three case studies. Obviously, the tensile and compressive-shear mixed-mode fracture mode can be reproduced realistically, and the efficient quadtree grids can be utilized directly, making the efficiency to be optimized by more than 75% in representative cases. More potential for practical applications would be further elucidated with extending the proposed method to three-dimensional.

1. Introduction

The deterioration of mechanical properties in materials results from fracturing, a common occurrence in various fields involving infrastructure, aerospace, power generation, and mechanical engineering. Fracture plays a significant role in localized structural failure, which can ultimately result in catastrophic destruction of entire structures. Therefore, to ensure safety, implement reinforcement measures, and mitigate risks, accurately identifying the location of structural cracks and capturing their gradual expansion are essential. However, structural damage and destruction remain a formidable issue in the field of engineering science throughout the 21st century [1]. This subject has attracted scholarly attention in recent years, with extensive research focused on developing theories and methods at the forefront of international investigations.

The primary techniques presently used for studying damage and fractures in rock-like materials are Peridynamics (PD), Discrete Element Method (DEM), eXtended Finite Element Method (XFEM), and Cohesive Zone Model (CZM). Representative studies include the following: Originating from the seminal works of Silling, S. A. et al. [2], PD has been enhanced and adapted for fracture analyses in rock-like materials [3,4].

DEM, created by Cundall et al. [5], could model the micro-behaviors of granular substances. By implementing meticulous enhancements and refinements [6–8], DEM has been capable of conducting precise cracking analyses of rock-like materials. Introduced by Belytschko et al. [9], XFEM has been utilized by researchers [10–12] to investigate the deformation characteristics and performance degradation of rock-like components. Originating from the seminal works of Barenblatt [13] and Dugdale [14], applications of CZM to rock fracture have been explored in subsequent studies [15–17]. Furthermore, derived from the F-M variation principle [18], the Phase-Field Model (PFM) has garnered significant attention since its development [19–22]. Researchers have achieved substantial progress in “energy anisotropic” [22–24] and the simulation of shear fracture [25–28]. Recent advancements in several DPFMs [29–38] have facilitated the modelling of mixed-mode fracture in rock. Remarkably, considering the influence of cohesion and internal friction angles on shear fracture, Xu et al. [39] introduced a DPFM for mixed-mode fracture according to the triple shear energy criterion, which accurately assesses fracture in rock. However, the PFM necessitates dense mesh to accurately capture high-gradient changes adjacent to cracks [32,40–43]. Consequently, considerable computational costs are inevitable, making new requirements and challenges to traditional

^{*} Corresponding author.

E-mail address: chenkai@dlut.edu.cn (K. Chen).

<https://doi.org/10.1016/j.tafmec.2025.104916>

Received 7 October 2024; Received in revised form 1 March 2025; Accepted 2 March 2025

Available online 12 March 2025

0167-8442/© 2025 Elsevier Ltd. All rights are reserved, including those for text and data mining, AI training, and similar technologies.

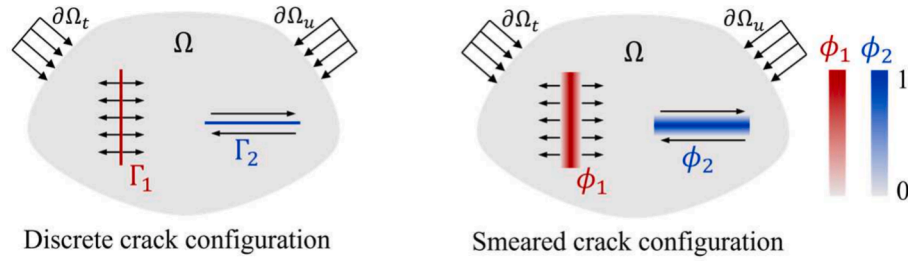


Fig. 1. Double-phase-field approximation.

analysis algorithms have emerged.

The adoption of cross-scale meshing has notably reduced computational demands while maintaining accuracy. Various element techniques, such as the Multi-Point Constraint Method [44–46], Polygonal Finite Element Method [47–49], and SBFEM, have been proposed to facilitate application. Among these, the SBFEM, pioneered by Song and Wolf [50–55], is distinguished by its semi-analytical property, which provides precise modeling of complex elements and has been widely recognized across different engineering disciplines. For instance, Chen et al. [56] enhanced the efficiency of dynamic analyses in metro structure by combining the SBFEM with FEM, utilizing Octree and element similarity technology. Ye et al. [57] investigated the interplay between the plate and multi-layered foundation using SBFEM-FEM techniques. Additionally, Zhao et al. [58] and Zhang et al. [59–61] have effectively utilized SBFEM to address complex challenges in soil mechanics, advancing the understanding of soil-structure interactions. Liu et al. creatively adopted SBFEM to simulate composite laminated shell container [62] and functionally graded sandwich beam [63]. Furthermore, Jiang et al. [64] created an innovative artificial intelligence method that interact in SBFEM, enabling efficient preventative maintenance procedures. The SBFEM has also been used in the analysis of various engineering structures [65–68], and recent studies have combined SBFEM with PFM for precise crack analysis across several scientific fields [41,69–74].

Nevertheless, the existing SBFEM-PFM coupling methods fall short in effectively addressing mixed-mode fractures. To alleviate the limitation, the “double-phase-field method” and “subdomain block Hammer integration” have been incorporated into SBFEM, forming a robust SBFEM-DPFM algorithm designed for analyzing mixed-mode fractures in rock-like materials. Employing the self-developed finite element software GEODYNA, built on object-oriented programming principles, the coupled SBFEM-DPFM simulation framework was built. The performance of algorithm has been assessed using traditional examples. The cracking process in rock components with various pre-existing cracks was precisely simulated. Moreover, the progressive mesh refinement techniques enabled rapid translation of the element size, substantially improving the efficiency of analyzing mixed-mode fractures in rock-like materials.

The paper is organized as follows: The DPFM based on the triple shear energy criterion is presented in Section 2. The formulations of the SBFEM-DPFM, the implementation details of the splitting block Hammer integration scheme, and the program design and integration are provided in Section 3. Classical examples used to validate the accuracy of the proposed approach are presented in Section 4. Meanwhile, the proposed method is verified by conducting intricate cracking examples, enhancing computational efficiency, and demonstrating its proficient predictive capability in complex fracture nucleation, propagation,

coalescence, and branching. Finally, the work is concluded in Section 5.

2. Double-phase-field model for tensile and compressive-shear fracture

2.1. Regularization of crack topology

Two mutually independent field functions are provided to portray tensile and shear fracture. For a solid Ω with a boundary $\partial\Omega$, the tensile and shear crack represented by the discrete and smeared crack configuration are depicted in Fig. 1. In the smeared crack configuration of the phase-field, the field function $\phi(x)_{1,2} = 1$ represents the destroyed material while $\phi(x)_{1,2} = 0$ represents the intact material.

The employed phase-field function for characterizing the smeared crack configuration is as follows:

$$\phi(x)_{1,2} = e^{\frac{-|x-x\Gamma_{1,2}|}{l_0}} \quad (1)$$

where l_0 denotes the characteristic length.

The fracture surface density function is formed [22] as:

$$\gamma(\phi_i, \nabla\phi_i)_{1,2} = \frac{1}{2l_0} \left(\phi_i^2 + l_0^2 |\nabla\phi_i|^2 \right)_{i=1,2} \quad (2)$$

2.2. Energy functions

According to the F-M variational principle [18], the total potential energy W comprises three distinct components: the bulk strain energy W_ϵ , the external potential energy W_{ext} , and the fracture surface energy W_{d_i} . The relationship is expressed as

$$W = W_\epsilon + W_{d_i} - W_{ext} \quad (3)$$

The individual components of total potential energy are listed as follows:

$$W_\epsilon = \int_{\Omega} g(\phi) \psi_0(\epsilon) d\Omega \quad (4)$$

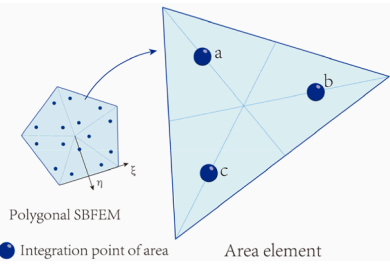
$$W_{ext} = \int_{\Omega} \bar{\mathbf{b}} \cdot \mathbf{u} dV + \int_{\partial\Omega} \bar{\mathbf{t}} \cdot \mathbf{u} dS \quad (5)$$

$$W_{d_i} = G_{c_i} \int_{\Omega} \gamma(\phi_i, \nabla\phi_i) d\Omega_{i=1,2} \quad (6)$$

where $g(\phi)$ is the degradation function, ϵ is the strain tensor, $\psi_0(\epsilon)$ is the nominal strain energy density, G_{c_i} is the critical energy release rate, $\bar{\mathbf{b}}$ and $\bar{\mathbf{t}}$ are the volume and boundary forces, respectively

The function $g(\phi)$ is expressed as

Table 1
Splitting block Hammer integration scheme.

Representation of integration point	Integration point	Area coordinate	Weight
 <p>Polygonal SBFEM</p> <p>Integration point of area</p> <p>Area element</p>	a	$\frac{2}{3} \frac{1}{6} \frac{1}{6}$	$\frac{1}{6}$
	b	$\frac{1}{6} \frac{2}{3} \frac{1}{6}$	$\frac{1}{6}$
	c	$\frac{1}{6} \frac{1}{6} \frac{2}{3}$	$\frac{1}{6}$

$$g(\phi) = (1 - \phi_1)^2 \cdot (1 - \phi_2)^2 \quad (7)$$

Substituting Eq. (4), (5), and (6) into Eq. (3) yields the total potential energy equation

$$W(\mathbf{u}, \phi_1, \phi_2) = \int_{\Omega} g(\phi) \psi_0(\epsilon) dV + G_{c1} \int_{\Omega} \gamma(\phi_1, \nabla \phi_1) dV + G_{c2} \int_{\Omega} \gamma(\phi_2, \nabla \phi_2) dV - \int_{\Omega} \bar{\mathbf{b}} \cdot \mathbf{u} dV + \int_{\partial\Omega} \bar{\mathbf{t}} \cdot \mathbf{u} dS \quad (8)$$

2.3. Governing equations

According to the principle of total potential energy minimization, the variation of the total potential energy $W(\mathbf{u}, \phi_1, \phi_2)$ are taken with respect to the displacement field \mathbf{u} and the phase field ϕ_i $i = 1, 2$, namely:

$$\begin{aligned} \delta W(\mathbf{u}, \phi_1, \phi_2) = & \int_{\partial\Omega} [(1 - \phi_1)^2 \cdot (1 - \phi_2)^2 \sigma \cdot \mathbf{n} - \bar{\mathbf{t}}] \delta \mathbf{u} dS - \int_{\Omega} \{ \nabla \cdot [(1 - \phi_1)^2 \cdot (1 - \phi_2)^2 \sigma] + \bar{\mathbf{b}} \} \delta \mathbf{u} dV \\ & + \int_{\Omega} [\frac{G_{c1}}{l_0} \phi_1 + (\phi_1 - 1) \cdot \sigma : \epsilon - G_{c1} l_0 \Delta \phi_1] \delta \phi_1 dV + \int_{\Omega} [\frac{G_{c2}}{l_0} \phi_2 + (\phi_2 - 1) \cdot \sigma : \epsilon - G_{c2} l_0 \Delta \phi_2] \delta \phi_2 dV \\ & + \int_{\partial\Omega} G_{c1} l_0 \nabla \phi_1 \cdot \mathbf{n} \delta \phi_1 dS + \int_{\partial\Omega} G_{c2} l_0 \nabla \phi_2 \cdot \mathbf{n} \delta \phi_2 dS \\ & = 0 \end{aligned} \quad (9)$$

where σ is the nominal stress tensor, and \mathbf{n} is the unit vector in the direction of the outward normal to the boundary.

Through the above variation, the fundamental equations and boundary conditions of the DPFM are obtained as follows:

$$\begin{cases} \nabla(1 - \phi_1)^2 \cdot (1 - \phi_2)^2 \sigma + \bar{\mathbf{b}} = 0, & \Omega \\ (1 - \phi_1)^2 \cdot (1 - \phi_2)^2 \sigma \cdot \mathbf{n} = \bar{\mathbf{t}}, & \partial\Omega \\ 2(\phi_1 - 1)\psi_1(\epsilon) + \frac{G_{c1}}{l_0} (\phi_1 - l_0^2 \nabla^2 \phi_1) = 0, & \Omega \\ 2(\phi_2 - 1)\psi_2(\epsilon) + \frac{G_{c2}}{l_0} (\phi_2 - l_0^2 \nabla^2 \phi_2) = 0, & \Omega \\ \nabla \phi_1 \cdot \mathbf{n} = 0, & \partial\Omega \\ \nabla \phi_2 \cdot \mathbf{n} = 0, & \partial\Omega \end{cases} \quad (10)$$

To prevent fracture healing, Miehe et al. [21] replaced $\psi_i(\epsilon)_{i=1,2}$ with H_i $i = 1, 2$ in Eq. (10). The expression for the variable H_i $i = 1, 2$ is outlined as follows:

$$H_i = \max_{t \in (0, T)} \{ \psi_i(\epsilon(\mathbf{x}, t)) \}_{i=1,2} \quad (11)$$

In the PFM for mixed-mode brittle fractures modified from the triple shear energy criterion, which Xu et al. [39] suggested, the tensile portion of the volumetric strain energy H_1 depends on the phase-field ϕ_1 as follow:

$$H_1(\epsilon) = \max_{t \in (0, T)} \left\{ (1 - \phi_1)^2 \frac{\lambda}{2} \langle \text{tr}(\epsilon) \rangle_+^2 + \frac{\lambda}{2} \langle \text{tr}(\epsilon) \rangle_-^2 \right\} \quad (12)$$

where λ represents the first Lamé constant, $\text{tr}(\epsilon)$ represents the trace of strain tensor matrix. and $\langle x \rangle_{\pm} = (x \pm |x|)/2$. Additionally, the shear strain energy $H_2(\epsilon)$ partitioned into the tensile shear component and the compressive shear component as follows:

$$H_2(\epsilon) = \max_{t \in (0, T)} \{ \psi_{dev}^+ + R \psi_{dev}^- \} \quad (13)$$

The threshold function R for determining the generation of

compressive-shear fracture is defined by the equation

$$\begin{cases} R = 1, \sum_{i=j+1}^3 \sum_{j=1}^2 \frac{1}{2\mu} \left(\frac{\sigma_j - \sigma_i}{2\cos\theta_{ji}} + \frac{\sigma_j + \sigma_i}{2} \tan\theta_{ji} \right)^2 \geq \frac{c^2}{\mu} \\ R = 0, \sum_{i=j+1}^3 \sum_{j=1}^2 \frac{1}{2\mu} \left(\frac{\sigma_j - \sigma_i}{2\cos\theta_{ji}} + \frac{\sigma_j + \sigma_i}{2} \tan\theta_{ji} \right)^2 \leq \frac{c^2}{\mu} \end{cases} \quad (14)$$

where μ is the second Lamé constant, σ_i and σ_j are principal stresses. The θ_{ji} represent the three friction angles on the yield surface.

Definitions for the tensile shear strain energy ψ_{dev}^+ and the compressive shear strain energy ψ_{dev}^- are given as

$$\psi_{dev}^+ = \mu \text{tr}(\epsilon_+^2) \quad (15)$$

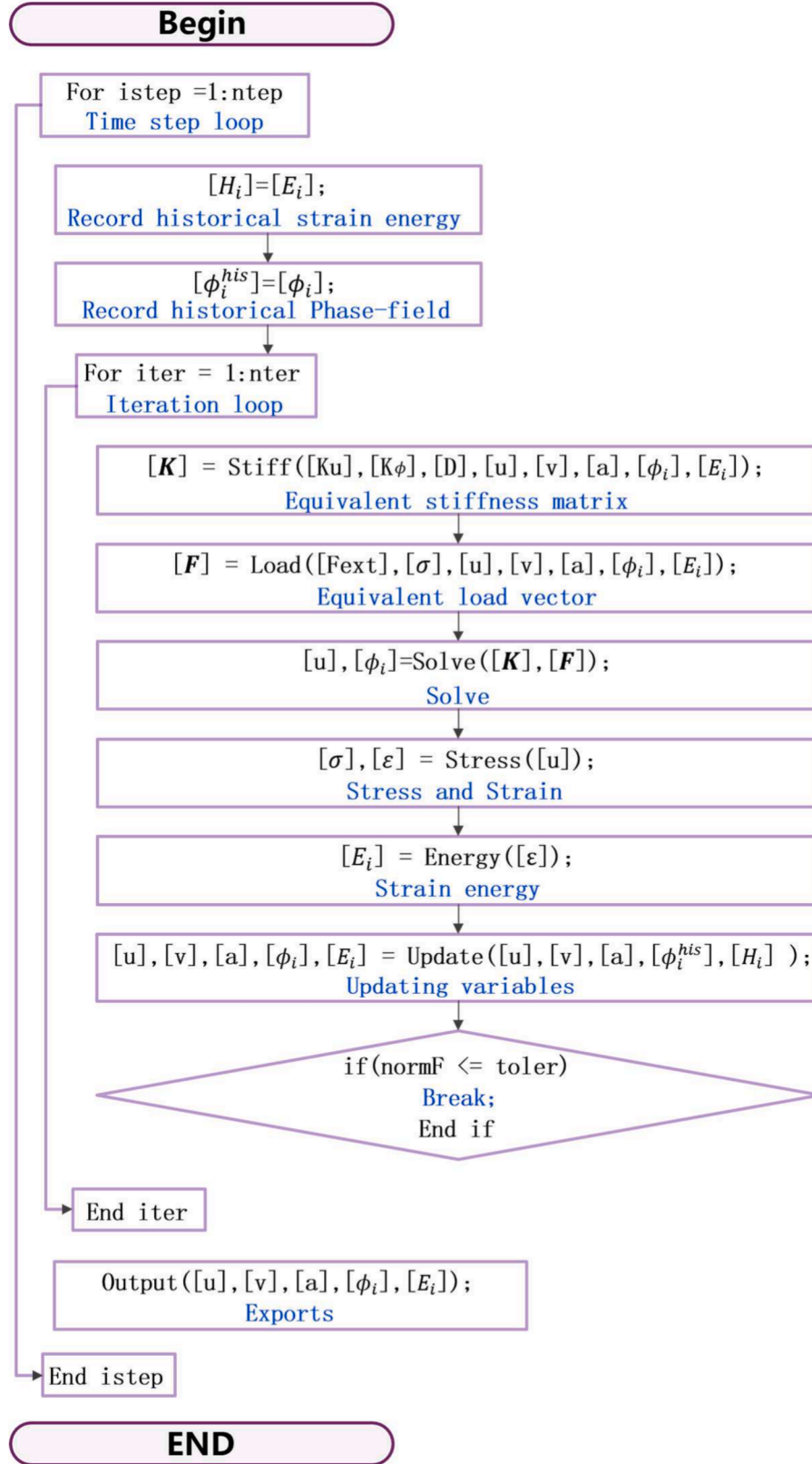


Fig. 2. Program implementation framework.

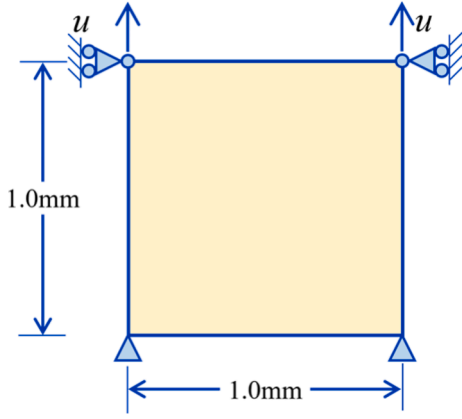
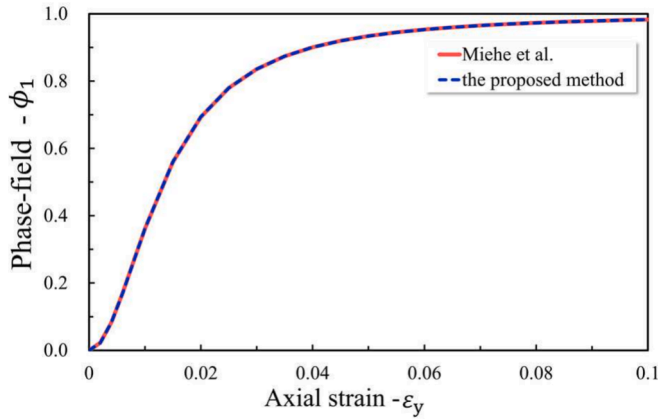


Fig. 3. Element and boundary conditions.

Fig. 4. Phase-field ϕ_1 -axial strain ε_y curve along with results by Miehe et al. [21].

$$\psi_{dev} = \sum_{i=j+1}^3 \sum_{j=1}^2 \frac{1}{2\mu} \left\langle \frac{\mu(\varepsilon_{ip} - \varepsilon_{jp})}{\cos\theta_{ji}} + [\lambda(\varepsilon_{1p} + \varepsilon_{2p} + \varepsilon_{3p}) + \mu(\varepsilon_{ip} + \varepsilon_{jp})] \tan\theta_{ji} - c \right\rangle_+^2 \quad (16)$$

where ε_+ is the positive part of strain tensor, $\varepsilon_{ip} = \langle \varepsilon_i \rangle_+$, and $\varepsilon_{jp} = \langle \varepsilon_j \rangle_-$. The ε_i and ε_j are principal strains. The c indicates cohesion.

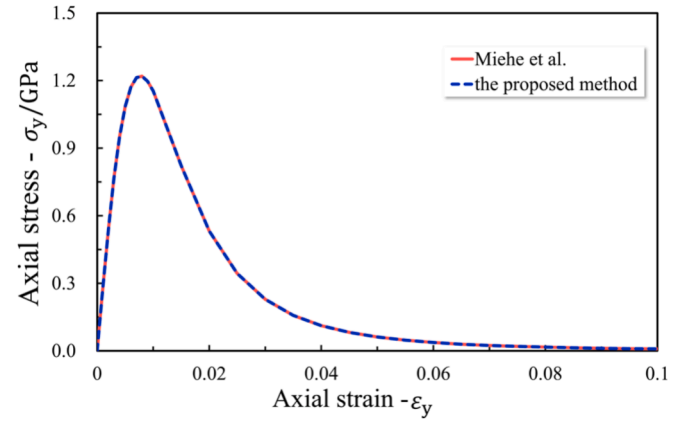
3. Numerical implementation

3.1. Coupling element development

Pioneered by Song and Wolf [50–55], the SBFEM has undergone extensive development, marking significant milestones across various research domains. As the existing literature on the displacement field is extensive, this paper will not discuss it further. The SBFEM-PFM, as proposed by Hirshikesh et al. [41], has been widely embraced by the research community [69–73,75,76]. This section succinctly presents the equations of SBFEM-DPFM as an enhancement of SBFEM-PFM.

3.2. Element shape function

The SBFEM equations for the DPFM are presented as follows:

Fig. 5. Axial stress σ_y -axial strain ε_y curve along with results by Miehe et al. [21].

$$G_c l_0 [E_{0\phi} \xi^2 \phi(\xi)_{,\xi\xi} + (E_{0\phi} + E_{1\phi}^T - E_{1\phi}) \xi \phi(\xi)_{,\xi} - E_{2\phi} \phi(\xi)] + \left[\frac{G_{ci}}{l_0} + 2H_i \right] \xi^2 M_\phi = \xi^2 P_{\phi i=1,2} \quad (17)$$

The coefficient matrices in Eq. (17) are delineated as follows:

$$\begin{aligned} E_{0\phi} &= \int_{\eta} \mathbf{B}_{1\phi}^T(\eta) \mathbf{B}_{1\phi}(\eta) \mathbf{J}(\eta) d\eta \\ E_{1\phi} &= \int_{\eta} \mathbf{B}_{2\phi}^T(\eta) \mathbf{B}_{1\phi}(\eta) \mathbf{J}(\eta) d\eta \\ E_{2\phi} &= \int_{\eta} \mathbf{B}_{2\phi}^T(\eta) \mathbf{B}_{2\phi}(\eta) \mathbf{J}(\eta) d\eta \\ \mathbf{M}_\phi &= \int_{\eta} \mathbf{N}_\phi^T(\eta) \mathbf{N}_\phi(\eta) \mathbf{J}(\eta) d\eta \\ \mathbf{P}_{\phi i} &= 2H_i \int_{\eta} \mathbf{N}_\phi^T(\eta) \mathbf{J}(\eta) d\eta \quad i=1,2 \end{aligned} \quad (18)$$

where $\mathbf{N}_\phi(\eta)$ and $\mathbf{J}(\eta)$ denote the shape function and Jacobian matrix, respectively, for the circumferential line element.

The matrices $\mathbf{B}_{1\phi}$ and $\mathbf{B}_{2\phi}$ in the above equation are given by

$$\begin{aligned} \mathbf{B}_{1\phi}(\eta) &= \mathbf{b}_{1\phi}(\eta) \mathbf{N}_\phi(\eta) \\ \mathbf{B}_{2\phi}(\eta) &= \mathbf{b}_{2\phi}(\eta) \mathbf{N}_\phi(\eta)_{,\eta} \end{aligned} \quad (19)$$

where the matrices $\mathbf{b}_{1\phi}$ and $\mathbf{b}_{2\phi}$ are defined as below:

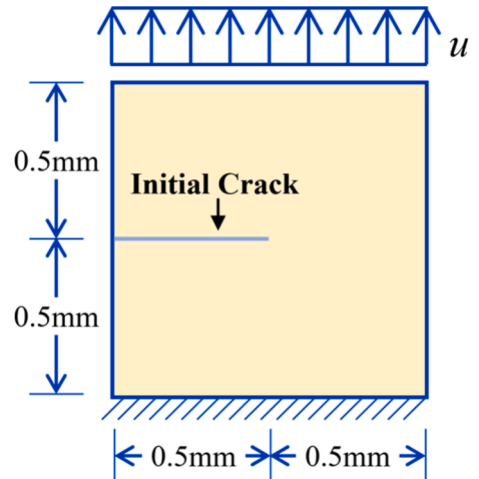


Fig. 6. Geometry and boundary conditions of a single-edge notched specimen.

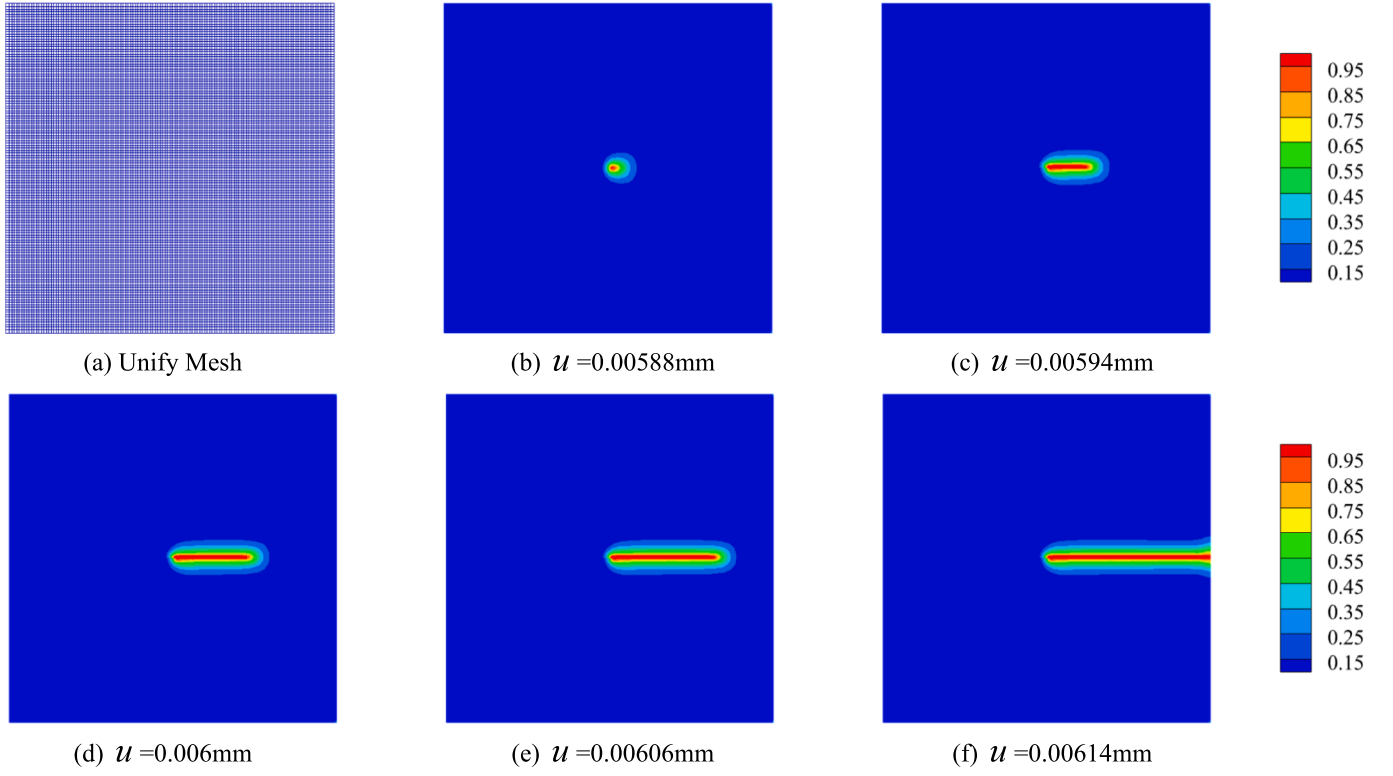


Fig. 7. Mesh scheme and phase-field evolution for the single-edge notched specimen.

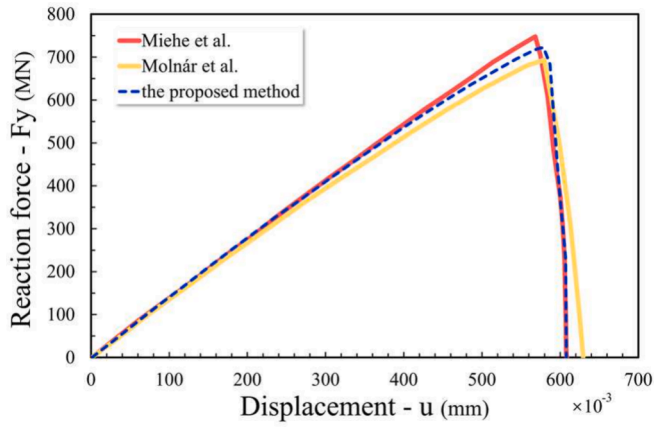


Fig. 8. Reaction force for the uniaxial tensile test with results of Miehe et al. [21] and Molnár et al. [97].

$$\begin{aligned} \mathbf{b}_{1\phi}(\eta) &= \frac{1}{J(\eta)} \begin{bmatrix} \mathbf{N}_{\phi}(\eta)_{,i} \mathbf{y}_b \\ -\mathbf{N}_{\phi}(\eta)_{,i} \mathbf{x}_b \end{bmatrix} \\ \mathbf{b}_{2\phi}(\eta) &= \frac{1}{J(\eta)} \begin{bmatrix} -\mathbf{N}_{\phi}(\eta) \mathbf{y}_b \\ \mathbf{N}_{\phi}(\eta) \mathbf{x}_b \end{bmatrix} \end{aligned} \quad (20)$$

where \mathbf{x}_b and \mathbf{y}_b indicate nodal coordinates of scaled boundary finite element.

When $\xi^2 P_{\phi i=1,2} = 0$, the Hamiltonian matrix \mathbf{Z}_{ϕ} is introduced to convert Eq. (17) into a first-order ordinary differential equation

$$\mathbf{Z}_{\phi} \mathbf{V}_{\phi} = \mathbf{V}_{\phi} \Lambda_{\phi} \quad (21)$$

Hamiltonian matrix \mathbf{Z}_{ϕ} is defined as

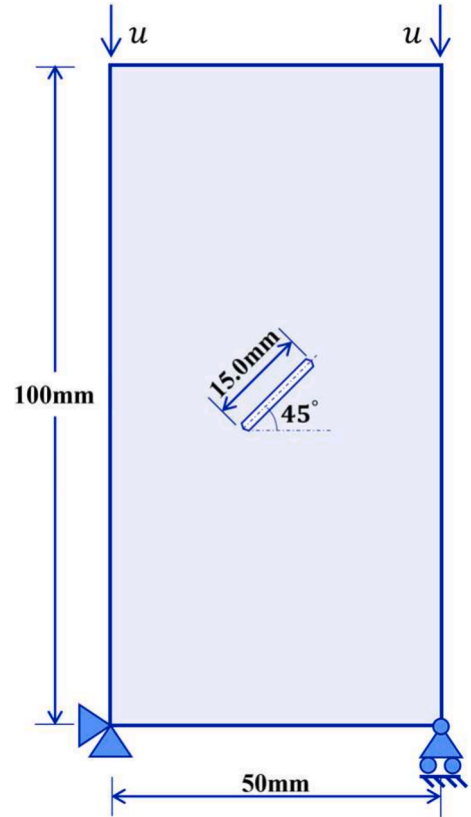


Fig. 9. Geometry and loading conditions of a rock specimen with a 45-degree angle initial crack.

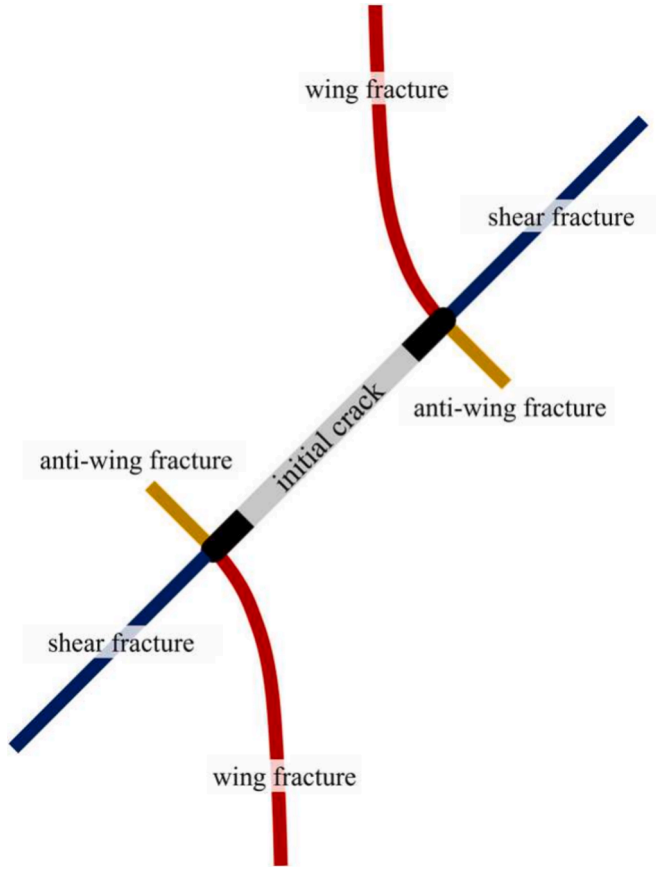


Fig. 10. Fracture patterns of a rock specimen with a 45-degree angle initial crack under uniaxial compression.

$$\mathbf{Z}_\phi = \begin{bmatrix} (\mathbf{E}_{0\phi})^{-1}(\mathbf{E}_{1\phi})^T & -(\mathbf{E}_{0\phi})^{-1} \\ \mathbf{E}_{1\phi}(\mathbf{E}_{0\phi})^{-1}(\mathbf{E}_{1\phi})^T - \mathbf{E}_{2\phi} & -\mathbf{E}_{1\phi}(\mathbf{E}_{0\phi})^{-1} \end{bmatrix} \quad (22)$$

By applying eigenvalue or Schur decomposition to the Hamiltonian matrix \mathbf{Z}_ϕ [77], the eigenvalues Λ_ϕ and eigenvectors \mathbf{V}_ϕ are obtained as follows:

$$\Lambda_\phi = \begin{bmatrix} \Lambda_\phi^+ & 0 \\ 0 & \Lambda_\phi^- \end{bmatrix} \quad (23)$$

$$\mathbf{V}_\phi = \begin{bmatrix} \mathbf{V}_{\phi 11} & \mathbf{V}_{\phi 12} \\ \mathbf{V}_{\phi 21} & \mathbf{V}_{\phi 22} \end{bmatrix} \quad (24)$$

The general solution for Eq. (17) can be obtained as follows:

$$\phi_i(\xi) = \mathbf{V}_{\phi 11} \xi^{-\Lambda_\phi} \mathbf{V}_{\phi 11}^{-1} \phi_i \quad i=1,2 \quad (25)$$

The phase-field $\phi_i(\xi, \eta)_{i=1,2}$ at any internal point within an element can be determined using the nodal phase-field ϕ_b at the boundary, as given by the following equation:

$$\phi_i(\xi, \eta) = \mathbb{N}_\phi(\xi, \eta) \phi_{bi=1,2} \quad (26)$$

Subsequently, the shape function for polygon elements $\mathbb{N}_\phi(\xi, \eta)$ is defined by the expression

$$\mathbb{N}_\phi(\xi, \eta) = \mathbf{N}_\phi(\eta) \mathbf{V}_{\phi 11} \xi^{-\Lambda_\phi} \mathbf{V}_{\phi 11}^{-1} \quad (27)$$

Similarly, the gradient of the DPF is characterized below:

$$\nabla \phi_i(\xi, \eta) = \mathbf{B}_{1\phi}(\eta) \phi_i(\xi)_{,\xi} + \xi^{-1} \mathbf{B}_{2\phi}(\eta) \phi_i(\xi)_{i=1,2} \quad (28)$$

Inserting Eq. (26) into Eq. (28) produces the derivative matrix of the phase-field shape function

$$\mathbf{B}_\phi(\xi, \eta) = \left[\mathbf{B}_{1\phi}(\eta) \mathbf{V}_{\phi 11} \left(-\Lambda_\phi^+ \right) + \mathbf{B}_{2\phi}(\eta) \mathbf{V}_{\phi 11} \right] \xi^{-\Lambda_\phi^+ - I} \mathbf{V}_{\phi 11}^{-1} \quad (29)$$

3.2.1. Splitting block Hammer integration scheme

The SBFEM is distinguished by its unique circumferential numerical and radial analytical characteristics, enabling excellent accuracy and the

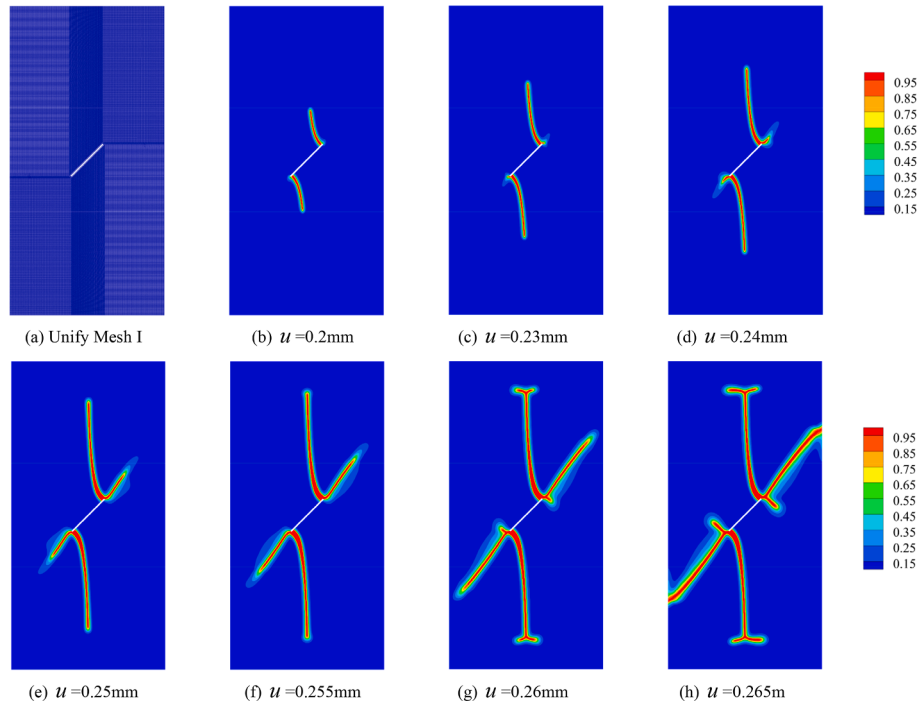


Fig. 11. Mesh scheme and phase-field evolution of the rock specimen with a 45-degree angle initial crack under uniaxial compression.

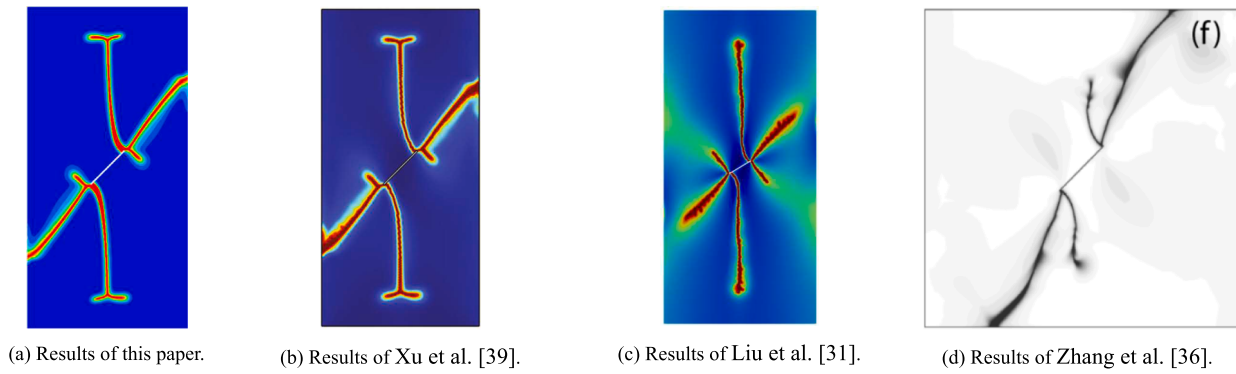


Fig. 12. Comparison with other researchers' results.



Fig. 13. Experimental result of Zhu et al. [108].

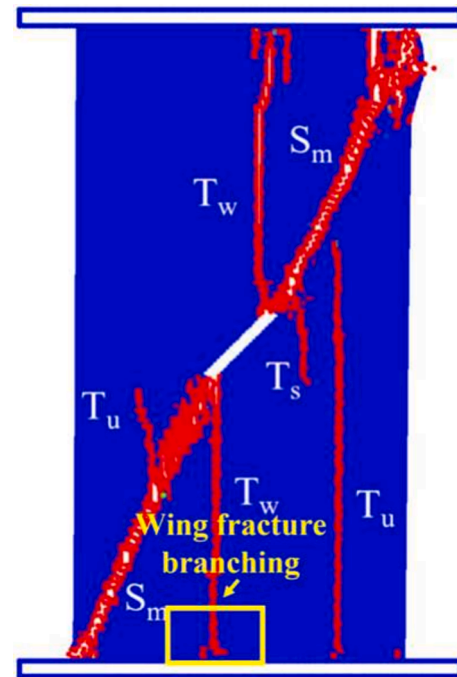


Fig. 14. Calculated results of Hu et al. [109].

compatibility for polygonal element. Nonetheless, calculating the phase-field within SBFEM continues to pose difficulties. It is commonly approximated by averaging the nodal phase-field [41,70–73,76]. The theory indicates that phase-field-related parameters inside the element are equal, constraining the characterization of the internal phase-field. Moreover, such simplification necessitates that the mesh size closely matches the crack dimension [41], placing considerable constraints on mesh configuration.

Further advancing the nonlinear SBFEM, the analytical integration-based solution was created by Ooi et al. [78] to tackle the inherent limitations of SBFEM. Although the solution is precise, it requires smaller element sizes and the complex configuration. Building upon this foundation, a more efficient nonlinear SBFEM was devised by Chen et al. [79], integrating constant stiffness eigenvalue decomposition with subdomain Hammer integration, thus enhancing the utility of SBFEM in

complex nonlinear geotechnical engineering. Expanding on the developments above, the subdomain block Hammer integration method is implemented to compute the internal DPF. As detailed in Eq. (30) and

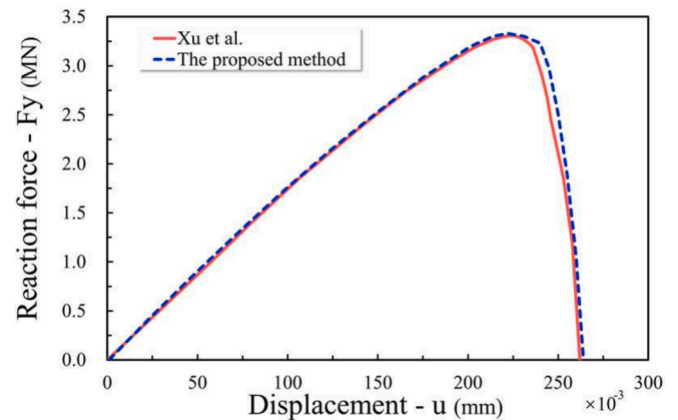


Fig. 15. Reaction force–displacement curve along with results by Xu et al. [39].

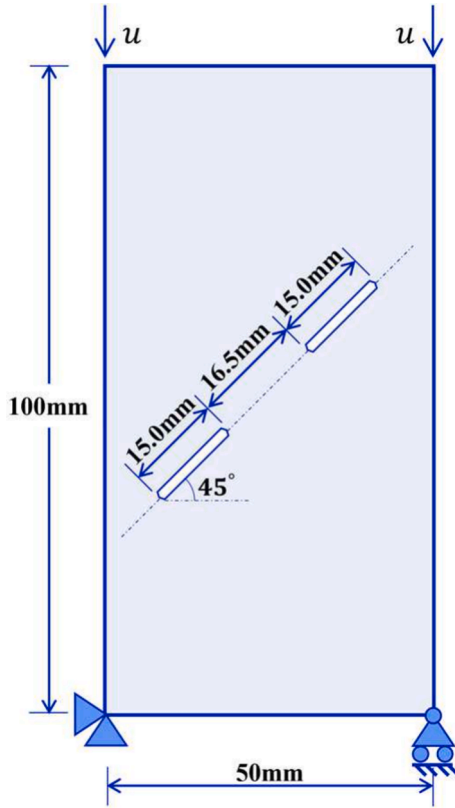


Fig. 16. Geometry and loading conditions of a rock specimen with double 45° initial cracks under uniaxial compression.

Table 1, the integration points within the triangular zones of each circumferential boundary line element are defined.

$$\iint_{\Omega_e} f(\xi, \eta) d\xi d\eta = \frac{1}{6} \left[f\left(\frac{2}{3}, \frac{1}{6}, \frac{1}{6}\right) + f\left(\frac{1}{6}, \frac{2}{3}, \frac{1}{6}\right) + f\left(\frac{1}{6}, \frac{1}{6}, \frac{2}{3}\right) \right] + o \quad (30)$$

The element stiffness matrices of displacement and DPF are obtained by integrating over the area integration points, as illustrated below:

$$\mathbf{K}_u^e = \sum_{s=1}^{3n} \left[(1 - \phi_{1s})^2 (1 - \phi_{2s})^2 + k \right] (\mathbf{B}_u(\xi, \eta))^T \mathbf{D} \mathbf{B}_u(\xi, \eta) \mathbf{A}_s \quad (31)$$

$$\mathbf{K}_{\phi_1}^e = \sum_{s=1}^{3n} \left\{ \left[\frac{G_{c1}}{l_0} + 2H_1(\varepsilon) \right] (\mathbb{N}_{\phi}(\xi, \eta))^T \mathbb{N}_{\phi}(\xi, \eta) + G_{c1} l_0 (\mathbb{B}_{\phi}(\xi, \eta))^T \mathbb{B}_{\phi}(\xi, \eta) \right\} \mathbf{A}_{si=1,2} \quad (32)$$

where n and $3n$ are the quantity of element edges and all integration points, respectively.

Similarly, the residue vectors of displacement and DPF are derived as below:

$$\mathbf{R}_u^e = \sum_{s=1}^{3n} \left[(1 - \phi_{1s})^2 (1 - \phi_{2s})^2 + k \right] (\mathcal{B}_u(\xi, \eta))^T \boldsymbol{\sigma}_s \mathbf{A}_s \quad (33)$$

$$\mathbf{R}_{\phi_1}^e = \sum_{s=1}^{3n} \left\{ \left[\frac{G_{c1}}{l_0} \phi_{1s} - 2(1 - \phi_{1s}) H_1(\varepsilon) \right] (\mathcal{N}_{\phi}(\xi, \eta))^T + G_{c1} l_0 (\mathcal{B}_{\phi}(\xi, \eta))^T \nabla \phi_{1s} \right\} \mathbf{A}_{si=1,2} \quad (34)$$

3.3. Program framework

The analysis of mixed-mode fracture in rock-like material presents multiple challenges, such as the interaction of different fields, discontinuous deformation, strong nonlinearity, and varying mesh size requirements. Given these complexities, no single numerical method suffices independently. Stability and efficiency are provided by the well-established FEM, while the solution of complex polygonal elements is excelled by the SBFEM, thus enhancing global-local analysis. Determining crack paths is autonomously carried out by the DPFM, eliminating the need for pre-established fracture criteria. The integration of these computational methods allows for the effective harnessing of their complementary strengths, thereby creating a robust approach for mixed-mode fracture analysis in rock-like materials.

3.3.1. Program access platform

Since starting in the 1990 s, our team has been dedicated to developing GEODYNA [80], a comprehensive software for geotechnical engineering. Comprising more than 300,000 lines of code, the system has been consistently enhanced to efficiently address a wide variety of infrastructure engineering requirements [56,65,81–95]. The present version of GEODYNA integrates several numerical techniques, including the FEM, the SBFEM, and the DPFM. Moreover, it provides intuitive interfaces for personalization, rendering it an essential platform for incorporating SBFEM-DPFM algorithm.

3.3.2. Program framework and implementation

This section generalizes the common attributes of the FEM-DPFM and SBFEM-DPFM setups based on object-oriented program. The class function library, interactive interfaces, and inheritance relationship are built to coordinate diverse elements. Program framework is as shown in Fig. 2.

The SBFEM-DPFM and FEM-DPFM algorithms leverage the CPU-parallel and GPU-solving capabilities of the GEODYNA software. Moreover, the integrated program facilitates the flexible access to the software's comprehensive rock-like constitutive package, load toolbox, and data-processing toolkit, thereby providing robust technical support for the investigation of mixed-mode fractures in rock-like materials.

3.3.3. Solution method

The coupled equation is addressed using a monolithic iterative approach. To improve solution performance, the off-diagonal part is neglected. This strategy was validated by existing research [28,83,96]. The detailed iterative equation is outlined as follows:

The Newton-Raphson method is applied to solving the nonlinear coupling equation in a monolithic iterative manner. The specific iteration format is expressed as:

$$\begin{Bmatrix} \mathbf{u} \\ \phi_1 \\ \phi_2 \end{Bmatrix}_{n+1} = \begin{Bmatrix} \mathbf{u} \\ \phi_1 \\ \phi_2 \end{Bmatrix}_n + \begin{bmatrix} \mathbf{K}_u & & \\ & \mathbf{K}_{\phi_1} & \\ & & \mathbf{K}_{\phi_2} \end{bmatrix}_n^{-1} \begin{Bmatrix} \mathbf{R}_u \\ \mathbf{R}_{\phi_1} \\ \mathbf{R}_{\phi_2} \end{Bmatrix}_n \quad (37)$$

The global stiffness matrices of the displacement field \mathbf{K}_u , the phase-field of tensile fracture \mathbf{K}_{ϕ_1} , and the phase-field of shear fracture \mathbf{K}_{ϕ_2} are derived by assembling the element stiffness matrices \mathbf{K}_u^e , $\mathbf{K}_{\phi_1}^e$, and $\mathbf{K}_{\phi_2}^e$ respectively.

4. Benchmark tests and numerical examples

4.1. Verification of accuracy

In this section, the precision of the proposed method is rigorously evaluated. To verify the accuracy of the element and the performance of the analysis for both single and mixed-mode fractures, three benchmark tests are conducted.

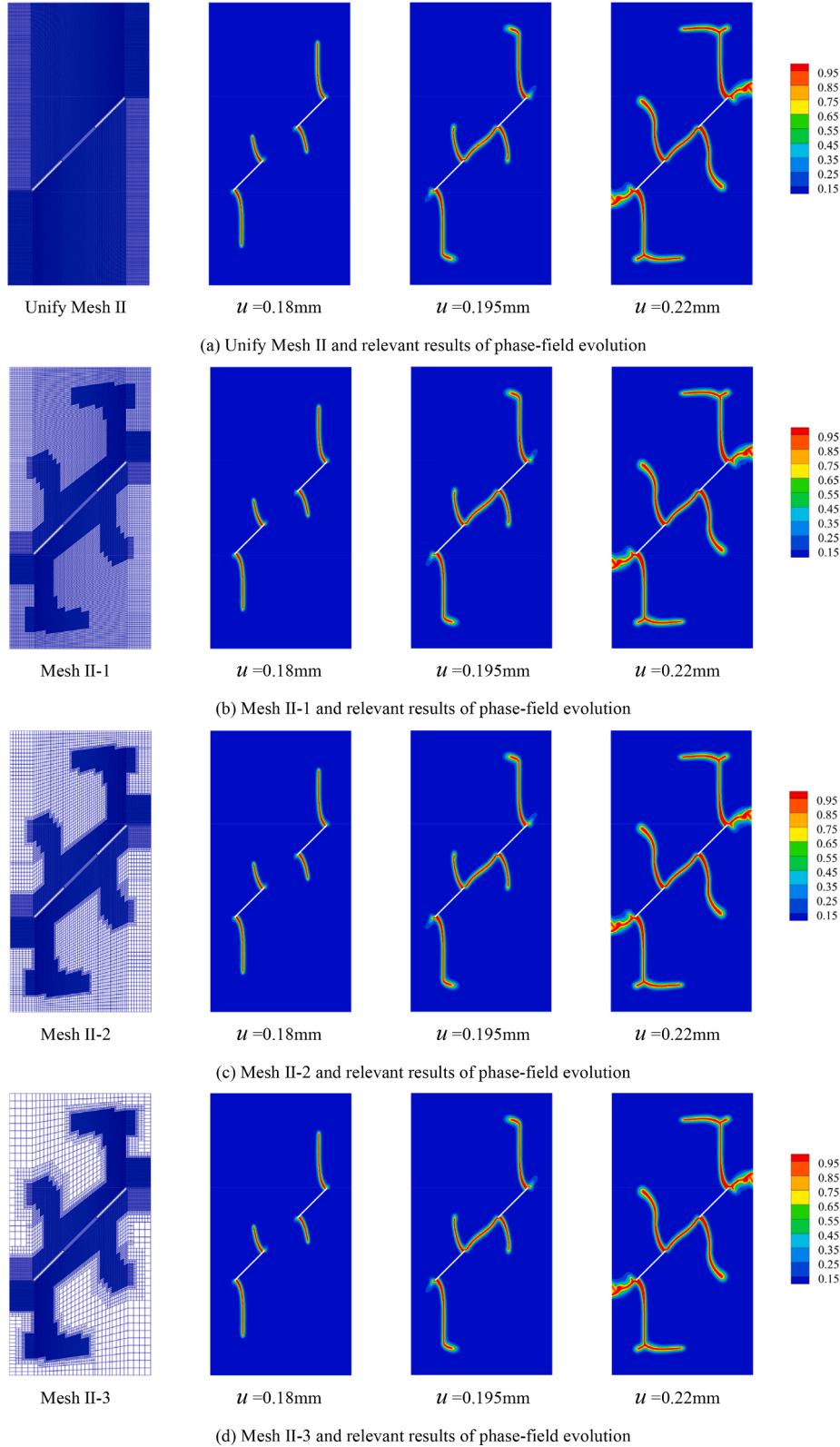


Fig. 17. Mesh and phase-field evolution of the rock specimen with double 45-degree angle initial cracks.

4.1.1. Tensile verification of element

The 2D plane strain element tensile test is conducted to verify the element precision, a widely recognized benchmark. The computational element is illustrated in Fig. 3, featuring a 1.0 mm by 1.0 mm element, vertical constraints at the bottom, and horizontal constraints on both sides. The progressive displacement load $\Delta u = 1e^{-4}$ mm is applied at the

top. To facilitate comparison, the degree of freedom (DOF) for the shear phase-field ϕ_2 is turned off in this example.

According to studies [21,42,97], the material parameters are determined as below: Young's modulus (E) of 210.0GPa; Poisson's ratio (ν) of 0.3, a critical energy release rate (G_c) of 5000 N/m; and a characteristic length (l_0) of 0.10 mm.

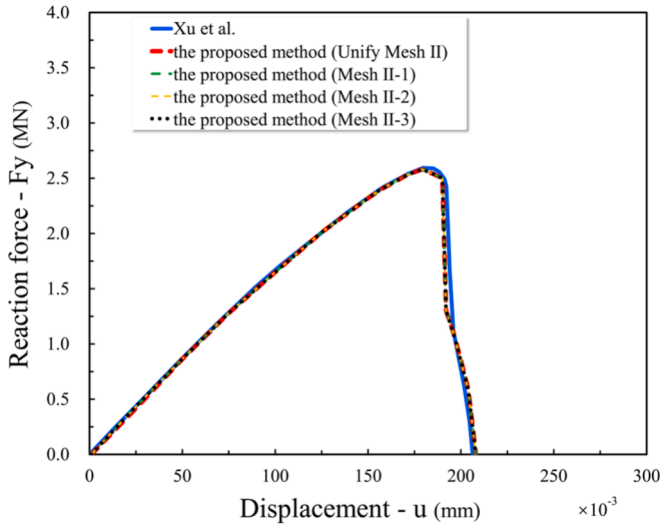


Fig. 18. Reaction force as a function of displacement curves of four mesh schemes along with results by Xu et al. [39].

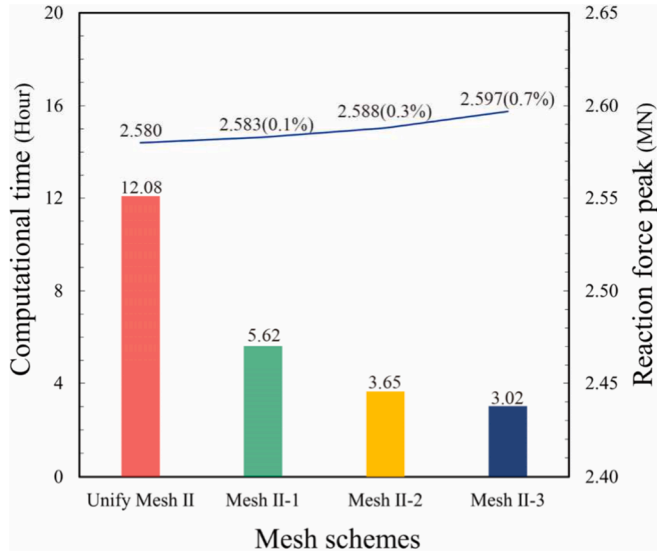


Fig. 19. Calculation time, reaction force peak, and relative error for different mesh schemes.

The tensile phase-field ϕ_1 –axial strain ε_y curve is illustrated in Fig. 4, and the axial stress σ_y –strain ε_y curve is depicted in Fig. 5. The phase-field progressively evolves under continuous vertical loading, gradually reducing in the element's stiffness. An apparent softening phenomenon is observed upon reaching peak stress. Following this, the element load-bearing capacity is gradually diminished. The results align with those reported by Miehe et al. [21], confirming the computational reliability of the quadrilateral phase-field SBF.

4.1.2. Tensile fracture evolution analysis

The geometry and boundary conditions, depicted in Fig. 6, comprise a specimen measuring 1.0 mm in width and height, with an initial 0.5 mm fracture on the left side. The model is constrained vertically at the bottom, and the displacement load of $\Delta u = 1e^{-4}$ mm is applied at the top with each incremental load step.

The material properties for the analysis include the elastic modulus (E) = 210 GPa; the Poisson's ratio (ν) = 0.3; the critical energy release rate (G_c) = 2,700 N·m; and the characteristic length (l_0) = 0.015 mm.

The computational model employs a uniform mesh size $h = 0.5l_0 =$

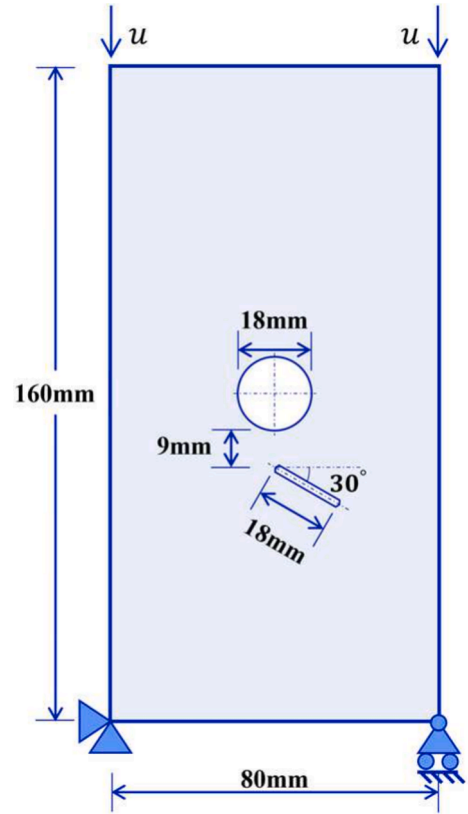


Fig. 20. Geometry and loading conditions of a rock specimen with a hole and an initial crack under uniaxial compression.

0.0075 mm, as recommended by Miehe et al. [21], incorporating 17,424 SBFEM-PFM elements. The shear phase-field degree of freedom, ϕ_2 , is deactivated to facilitate comparison.

Mesh scheme and phase-field evolution are presented in Fig. 7. As the displacement load increases to $u = 0.00588$ mm, the fracture is observed to nucleate and propagate along the direction of the initial crack. At $u = 0.00614$ mm, the fracture completely penetrates the specimen, leading to specimen failure. The curve of the vertical support reaction force as a function of vertical displacement is illustrated in Fig. 8. The force is increased with loading until the structure is seen to begin cracking, reaches a peak, and subsequently decreases as loading continues. Once the fracture has fully penetrated, the specimen become nonfunctional and is no longer able to support any load. The cracking process and vertical support reaction force curve generally concur with the results of Miehe et al. [21] and Molnár et al. [97]. Based on these findings, it is concluded that our approach accurately describes and predicts the tensile fracture phenomenon.

4.1.3. Mixed-mode fracture evolution analysis

The accuracy of the double-phase-field calculation is demonstrated through a uniaxial compression test on a rock specimen with an initial crack, a benchmark widely analyzed in prior studies [29,30,33,34,36–39,80,83,91,98–108].

The geometry and loading conditions are illustrated in Fig. 9. The model measures 50 mm in width and 100 mm in height, featuring a centrally located, prefabricated crack 15.0 mm long and 0.5 mm wide. The specimen is fixed vertically at the bottom and horizontally on the left side at its base. Each load increment involves the displacement of $\Delta u = -1.0e^{-3}$ mm applied at the top. The recognized fracture pattern is illustrated in Fig. 10. Initially, tensile stresses build up, resulting in wing fractures at the tips of the cracks. With increasing loading, the concentration of shear stress leads to the formation of two shear fractures that

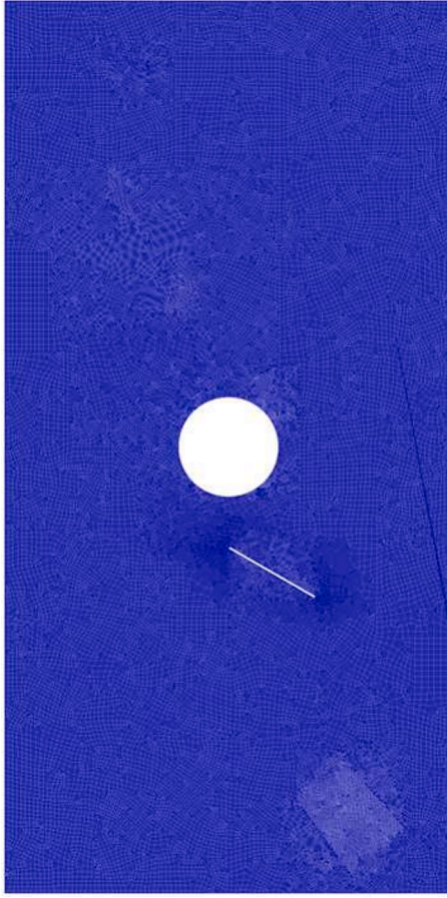


Fig. 21. Global fine mesh (Mesh II-4).

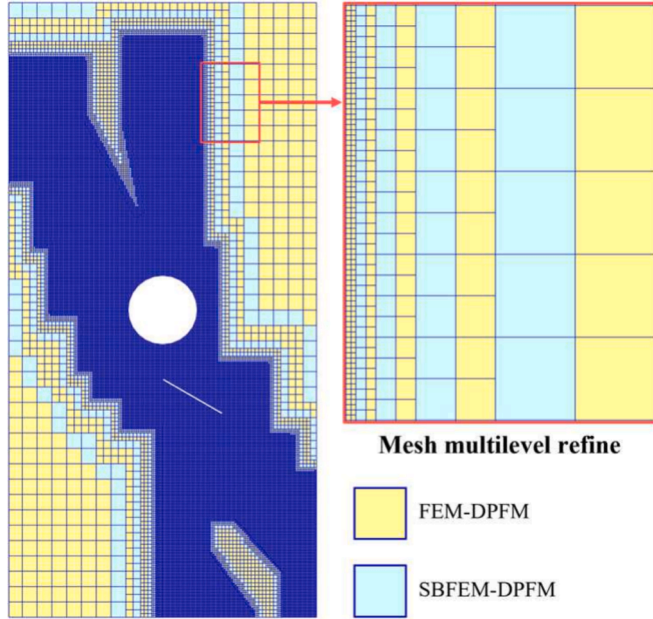


Fig. 22. Quadtree mesh and types of elements (Mesh II-5).

lie in parallel with the initial crack. As loading continues, anti-wing fractures nucleate and progress. Over time, the propagation and interaction of multiple fractures lead to a gradual reduction in the structural strength. Ultimately, the inability to bear the load results in a complete

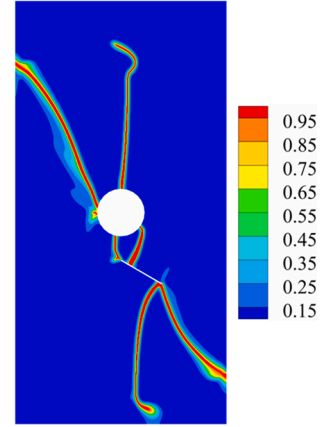


Fig. 23. Results of the global fine mesh with FEM-DPFM.

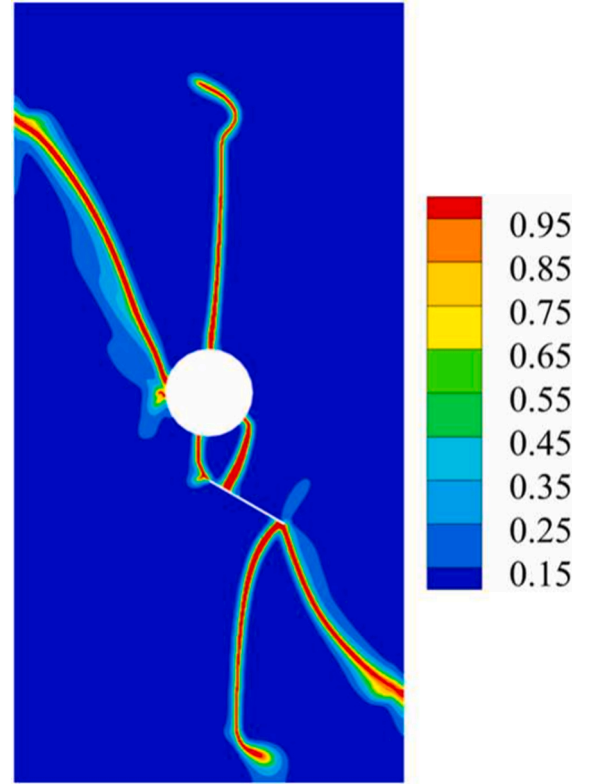


Fig. 24. Results of the Quadtree mesh with multiple numerical methods.

structure breakdown.

In order to demonstrate the accuracy of the proposed method in analyzing tensile and compressive-shear fracture, the same computational parameters as those employed by Xu et al. [39] are used. These parameters include: The Young's modulus (E) is 36.2GPa, the Poisson's ratio (ν) is 0.21, the critical energy release rates (G_{ci} , $i = 1, 2$) are 16 N/m for tension and 200 N/m for compressive shear, the length scale parameter (l_0) is 0.5, the cohesion (c) is 500 kPa, the frictional angles (θ_{13}) is 30-degree and (θ_{12}, θ_{23}) are 19.74-degree. The uniform parameters facilitate comparison with previous results, thereby improving the credibility of validation.

Following the minimum element size $h = 0.5l_0 = 0.25$ mm as recommended by Miehe et al. [22], the computational model was discretized with a uniform mesh size h across the entire domain, incorporating 17,424 SBFEM-DPFM elements.

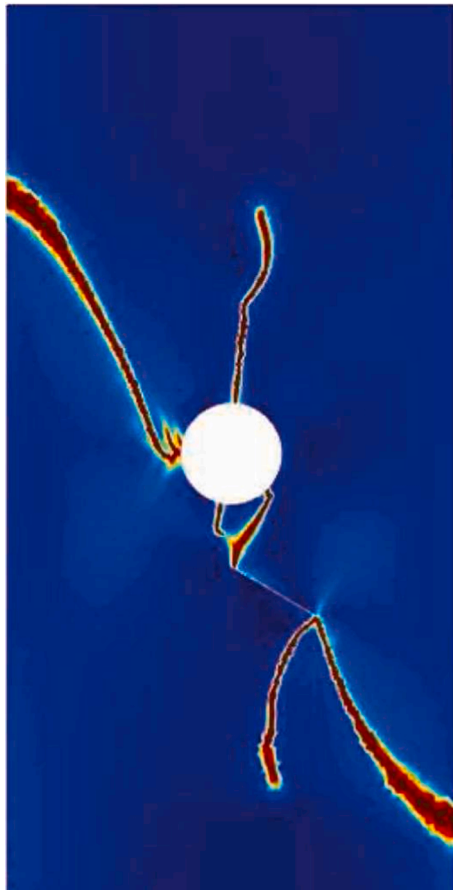


Fig. 25. Calculated results of Cao et al. [99].

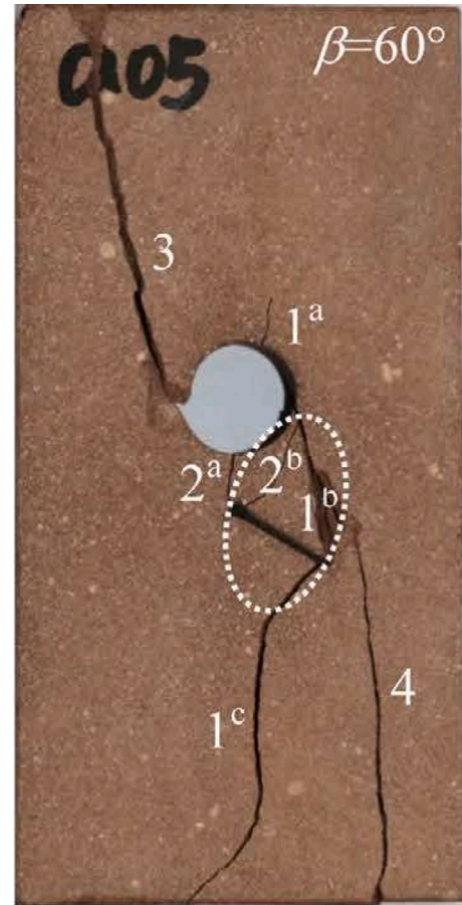


Fig. 26. Experimental results of Yin et al. [110].

The phase-field evolution is shown in Fig. 11. When the displacement load reaches $u = 0.2$ mm, wing fractures are initiated at the ends of the predefined crack, and shear fractures have not yet nucleated. At $u = 0.23$ mm, shear fractures are initiated at the tips of the predefined crack, driven by concentrated shear stresses, and progress along the direction of the initial crack with continued loading. As the vertical displacement increases to $u = 0.26$ mm, crack branching is commenced at the tips of the wing fractures, and shear fractures further evolve. Opposite the direction of the wing fractures, anti-wing fractures start to develop at the crack tips. Ultimately, when the applied load reaches $u = 0.265$ mm, the component fails due to the penetration of shear cracks.

The method replicates tensile and compressive-shear fractures in rock specimens with a 45-degree angle predefined crack, effectively capturing the fracture paths and evolution process. Comparative results align with the findings of Xu et al. [39], who utilized 207,092 triangular meshes, as shown in Fig. 12(b). Further comparisons with studies by Liu et al. [31] and Zhang et al. [36], presented in Fig. 12 (c) and (d), respectively, and experimental data from Zhu et al. [108] in Fig. 13, alongside computational results using SPH by Hu et al. [109] in Fig. 14, confirm the ability of the proposed method to simulate crack evolution and component failure mechanisms accurately.

Additionally, the comparison of vertical reaction force–displacement loading curves with those presented by Xu et al. [39], illustrated in Fig. 15, reveals that peak reaction forces are reached before the onset of shear fractures. Subsequently, the reaction force drops rapidly with increased loading, and the component loses all resistance once the shear fractures penetrate.

The cross-validation process, which involves the prediction of crack paths and resistance curves, yields result consistent with the findings of other researchers. The computational program developed is demonstrated reliability and stability in addressing tensile and compressive-

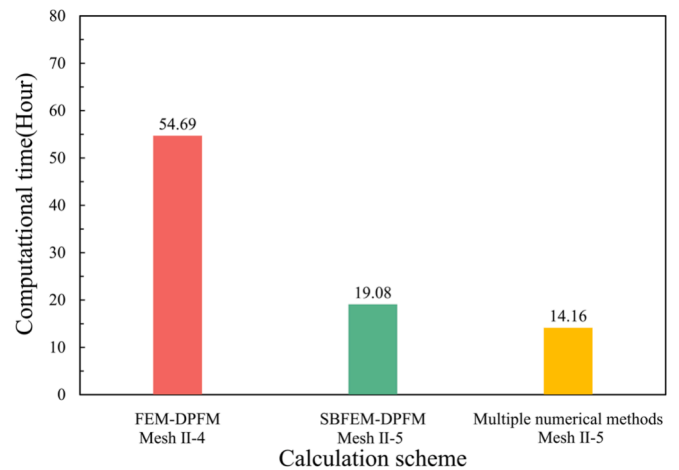


Fig. 27. Calculation time for different calculation schemes.

shear fractures in rock-like materials.

4.2. Optimization of computational efficiency in cross scale mesh and hybrid element methods

4.2.1. Cross scale mesh

The potential for enhanced efficiency through cross-scale mesh was investigated utilizing a specimen with dual 45° initial cracks, each 15 mm long and 0.5 mm wide, spaced 16.5 mm apart, as depicted in Fig. 16. The dimensions of the specimen were 50 mm in width and 100 mm in

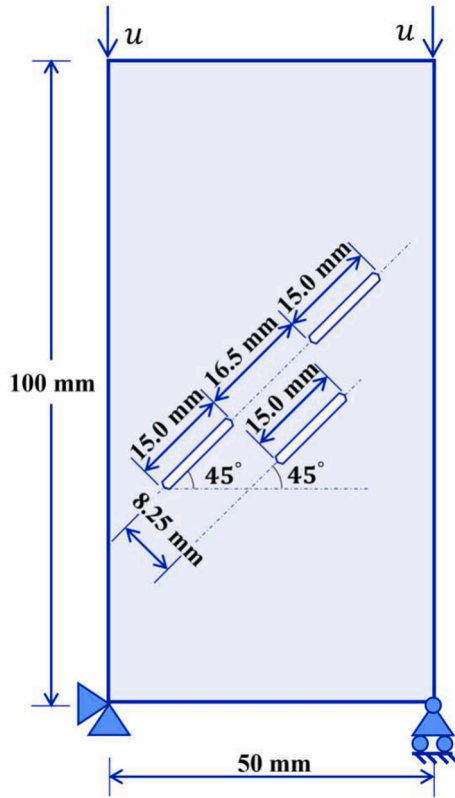


Fig. 28. Geometry and loading conditions of a rock specimen with three 45-degree angle initial cracks.

height. The model is constrained vertically at the bottom and horizontally on the left side at the bottom. Incremental displacement loads of $\Delta u = -1.0e^{-3}$ mm are applied at the top of the specimen for each load step. The material parameters set forth in Section 4.1.3 are consistently maintained.

Following the recommendations put forth by Miehe et al. [22], the computational model utilizes a uniform mesh size of $h = 0.5l_0 = 0.25$ mm throughout the entire domain. The model, designated as Unify Mesh II, comprises 103,184 SBFEM-DPFM elements. Numerical models with entire domain mesh sizes of $2h$, $4h$, and $8h$ are established to study the influence of mesh cross-scaling on the calculation performance. The mesh size of the models gradually increases in density within the fracture zone until it reaches the mesh size of h . The corresponding SBFEM-DPFM element counts are 58,296, 48,624, and 46,904, respectively. To simplify the presentation, the mesh schemes above are labeled as Mesh II-1, Mesh II-2, and Mesh II-3.

The calculation results using Unify Mesh II are depicted in Fig. 17(a). The wing fractures grow at the ends of the initial cracks upon reaching a vertical displacement load of $u = 0.18$ mm, and shear fractures start nucleating due to the shear stress concentration. As the vertical displacement reaches $u = 0.195$ mm, the expansion of wing fractures persists, and the shear fractures penetrate between the initial cracks in the direction of the extended initial cracks. Eventually, a crack penetrates the component and causes failure when the vertical displacement load reaches $u = 0.22$ mm.

Fig. 17 (b), (c), and (d) show the results of the phase-field calculated using Mesh II-1, Mesh II-2, and Mesh II-3, respectively. The calculation results obtained through progressive refinement mesh are consistent with those of full-domain fine-scale mesh. Simultaneously, the element counts are reduced by 43.5 %, 52.9 %, and 54.5 %.

The vertical reaction force-vertical displacement load curve, as presented in Fig. 18, corresponds with the findings of Xu et al. [39]. As the loading continues, the vertical reaction force increases gradually,

achieving its peak $atu = 0.18$ mm. $Atu = 0.195$ mm, the vertical bearing capacity decreases sharply due to the penetration of shear cracks at the center of model. When the vertical displacement reaches $u = 0.22$ mm, the structure loses its load-bearing capability as the development of shear fractures leads to a penetrating fracture throughout the component. In addition, Fig. 19 illustrates the computation time, reaction force peak, and relative error for different mesh schemes. The figure indicates that the combination of SBFEM-DPFM with mesh gradually refine technology increases the computational efficiency by 75 % while guaranteeing a relative error of less than 1 %. The comprehensive demonstration of SBFEM-DPFM as an effective approach for tensile and compressive-shear fracture analysis is presented above.

4.2.2. Integration of multiple numerical methods

The SBFEM enables high-precision solutions through a circumferential analytical-radial discretization approach. While it incurs a slightly higher computational cost compared to traditional *iso*-parametric elements, it supports complex polygonal elements and offers significant advantages for multi-scale meshing. In contrast, the *iso*-parametric element method is well-established and structurally simple. However, its limited by the simple geometry of the elements necessitates extensive manual intervention when constructing cross-scale meshes. The limitation becomes particularly apparent in the analysis of crack propagation in complex specimens. To address the technical challenge, the present study develops a coupled computational framework that integrates multiple methods: FEM-DPFM is employed for three-node and four-node elements, while SBFEM-DPFM is utilized for multi-node complex elements. Notably, the integration of SBFEM-DPFM and FEM-DPFM within a unified computational framework, coupled with efficient quadtree mesh discretization technique, further enhances computational efficiency.

A geometric model is established based on the work of Cao et al. [99] and Yin et al. [110], as depicted in Fig. 20. The model dimensions are $160 \text{ mm} \times 80 \text{ mm}$, with a central hole of 18 mm in diameter. An initial crack, 18 mm in length, 0.5 mm in width, and inclined at 30° , is located 9 mm below the bottom of the hole. The boundary conditions are as follows: vertical displacement is constrained at the bottom, horizontal displacement is restricted at the lower-left corner, and displacement loads $\Delta u = -2.0e^{-3}$ are applied incrementally at the top, with a total of 360 load steps.

The material parameters are as follows: The Young's modulus (E) is 12.63 GPa, the Poisson's ratio (ν) is 0.3, the critical energy release rates ($G_{ci=1,2}$) are 20 N/m for tension and 200 N/m for compressive shear, the length scale parameter (l_0) is 0.5 mm, the cohesion (c) is 500 kPa, the frictional angles (θ_{13}) is 30-degree and (θ_{12}, θ_{23}) are 19.74-degree.

The minimum mesh size $h = 0.5l_0 = 0.25$ is taken as recommended by Miehe et al. [22]. Two discretization models are constructed: a global fine mesh model (Mesh II-4, consisting of 198,553 elements) and a quadtree multi-scale mesh model (Mesh II-5, consisting of 99,674 elements), as shown in Fig. 21 and Fig. 22. The Mesh II-5 model includes 1,606 SBFEM-DPFM elements.

To evaluate the computational efficiency of the proposed method, three computational schemes are compared: (1) the Mesh II-4 using the FEM-DPFM solution, (2) the Mesh II-5 using the SBFEM-DPFM solution, and (3) the Mesh II-5 incorporating multiple numerical methods.

The failure patterns are presented in Fig. 23 and Fig. 24. Compared to the numerical simulations of Cao et al. [99], the results in this study exhibit a higher consistent with experimental data of Yin et al. [110] in regions 2a and 2b, as shown in Fig. 25 and Fig. 26. A comparison of the computational times for these three schemes, as shown in Fig. 27, demonstrates that the multiple numerical methods coupling system significantly enhances computational efficiency.

4.3. Crack evolution analysis of complex component

The mixed-mode crack evolution within a complex component is

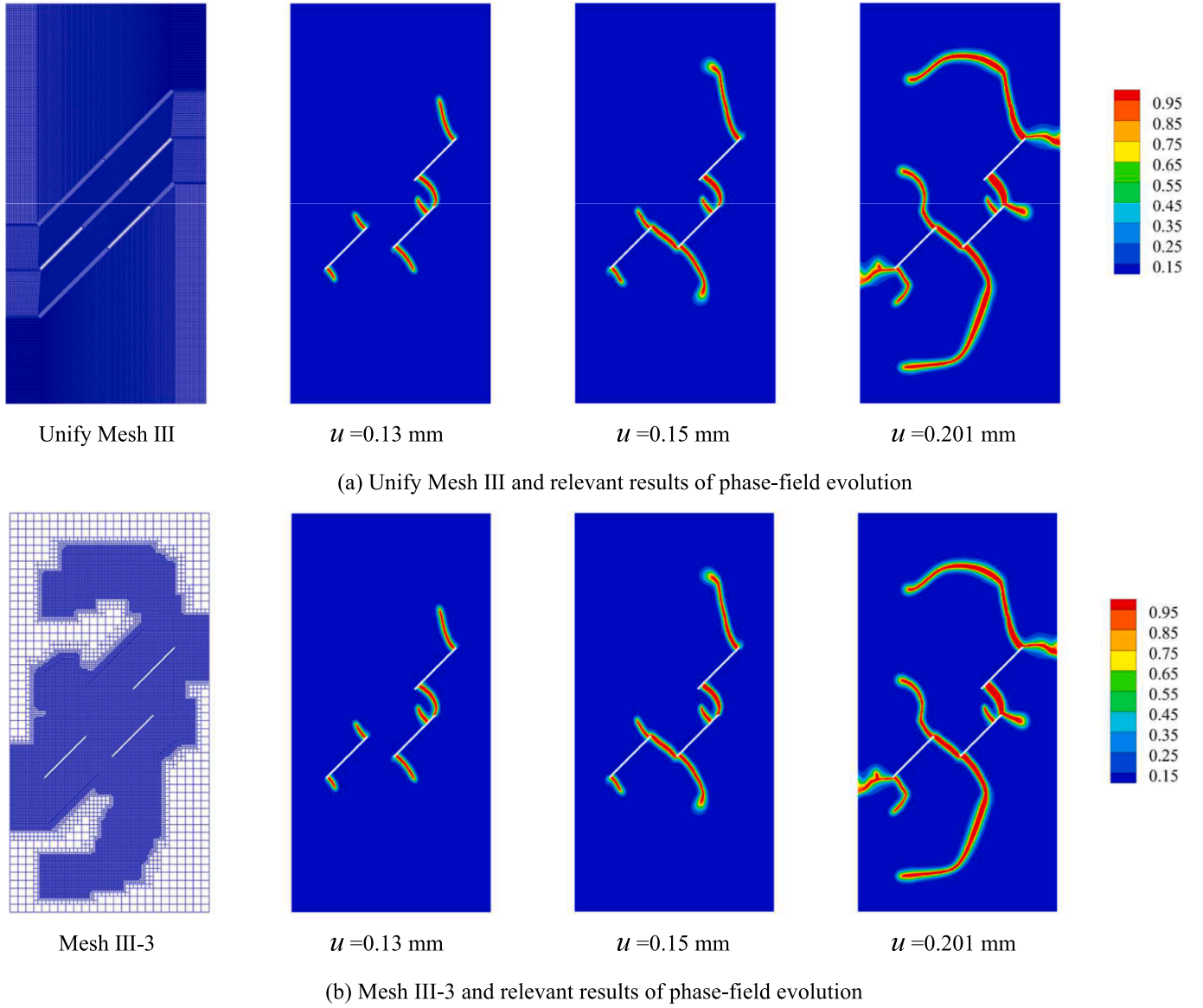


Fig. 29. Mesh schemes and phase-field evolution of the rock specimen with three 45-degree angle initial cracks under uniaxial compression.

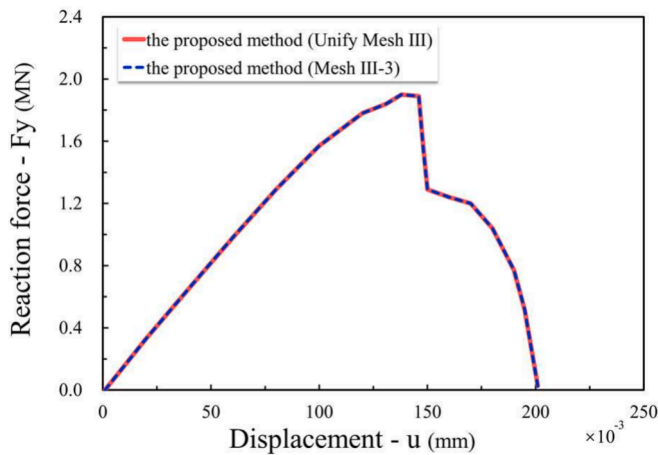


Fig. 30. Reaction force as a function of displacement curves of three 45-degree angle initial cracks under uniaxial compression.

examined as depicted in Fig. 28. The model incorporates three initial cracks positioned at 45-degree angles, each measuring 15.0 mm in length and 0.5 mm in width. The spacing between the adjacent side cracks is set at 16.5 mm, while the gap between the side cracks and the central crack is 8.25 mm. Constraints are applied vertically at the base of model and horizontally on the lower left side. Each incremental load step applies a displacement $\Delta u = -1.0e^{-3}$ mm at the top of the model. The material properties used align with those outlined in Section 4.1.3.

The geometric model was discretized with a mesh size h of the entire domain, according to the minimum element size $h = 0.5l_0 = 0.25$ mm proposed by Miehe et al. [22], with 102,040 SBFEM-DPFM elements, denoted as Unify Mesh III. Additionally, a sophisticated computational model has been configured with a global mesh size of $8h$. Within this model, the mesh density progressively increases across the fracture zone until achieving a mesh size of h . This model, which incorporates 46,303 SBFEM-DPFM elements, is labeled Mesh III-3.

The phase-field evolution process is illustrated in Fig. 29. At a displacement of $u = 0.13$ mm, wing fractures occur at the tips of the initial cracks due to tensile stress concentration, forming a penetrating crack between the two initial cracks on the right side. Upon reaching a vertical displacement of $u = 0.15$ mm, a shear-induced penetrating

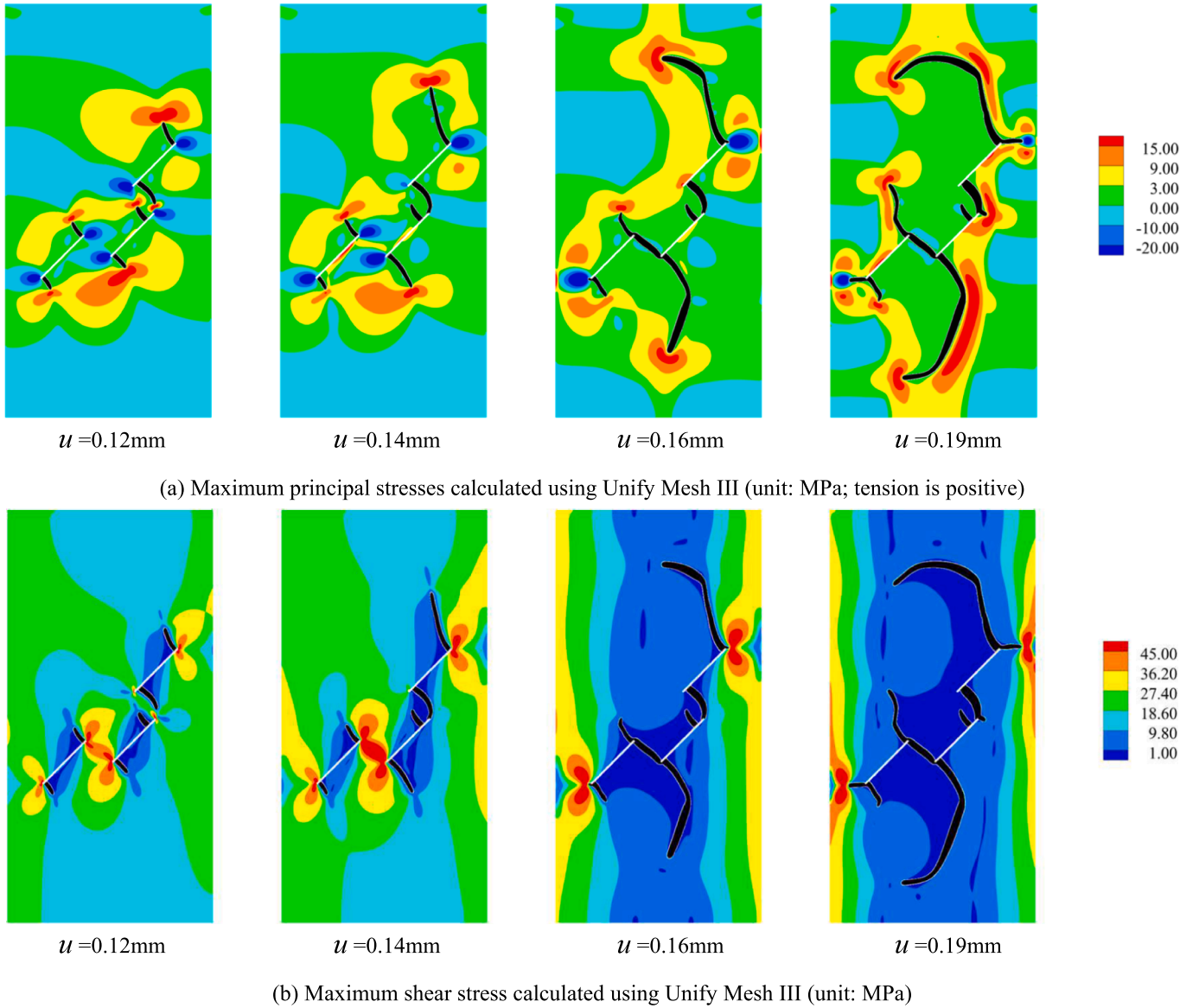


Fig. 31. Maximum principal stresses and shear stress of the rock specimen with three 45-degree angle initial cracks under uniaxial compression.

fracture develops between the bottom two initial cracks. At a displacement of $u = 0.201$ mm, shear fractures at the tips of the initial crack on both sides evolve into penetrating cracks, ultimately leading to component failure.

Fig. 29(b) illustrates the phase-field computed with Mesh III-3, and Fig. 30 portrays the vertical reaction force versus displacement load curve. Together, Fig. 29 and Fig. 30 validate that the computational outcomes derived through the progressively cross-scaling meshing outlined in this paper are consistent with those from Unify Mesh III. Furthermore, there is a notable 54.6 % reduction in total elements. These results demonstrate that integrating SBFEM-DPFM with multi-level mesh refinement technology can effectively reduce the computational burden.

The distribution of the maximum principal stress is shown in Fig. 31 (a). As the vertical displacement load reaches $u = 0.12$ mm, the maximum principal stress is released at the fracture location, predominantly concentrating at the wing crack tips. With an increment to a load of $u = 0.14$ mm, an interconnecting through-crack emerges between the right-side fractures. Subsequently, as the tensile fractures propagate, the maximum principal stress zones adapt to the evolution of the crack tips.

The distribution of the maximum shear stress is shown in Fig. 31 (b).

At a vertical displacement load of $u = 0.12$ mm, the stress concentrates predominantly at the ends of the initial cracks. As the load escalates to $u = 0.14$ mm, the shear stress concentration remains at the endpoints, and the value of the maximum shear stress increases, forming a noticeable stress concentration between the two initial cracks at the bottom. Upon reaching a load of $u = 0.16$ mm, the central part of the component loses its ability to resist shear, with stress being concentrated at the crack tips on both sides. As the loading progresses, through-crack forms, eventually leading to component failure.

Points A, B, and C have been selected as representative points to examine the evolution of stress within the component meticulously. The locations are illustrated in Fig. 32. At point A, between the two initial cracks on the right, the maximum principal stress peaks at a vertical load of $u = 0.12$ mm. As the wing cracks propagate, the stiffness at point A is significantly diminished, with the release of the maximum principal stress. Point B, positioned between the two initial cracks at the bottom, experiences a peak in maximum shear stress at a vertical displacement load of $u = 0.14$ mm. Subsequently, as the fracture penetrates, there is a rapid decline in the maximum shear stress. At point C, situated at the site of the shear fracture on the right side of specimen, the maximum shear stress is observed to reach its peak at $u = 0.175$ mm. As the shear fracture

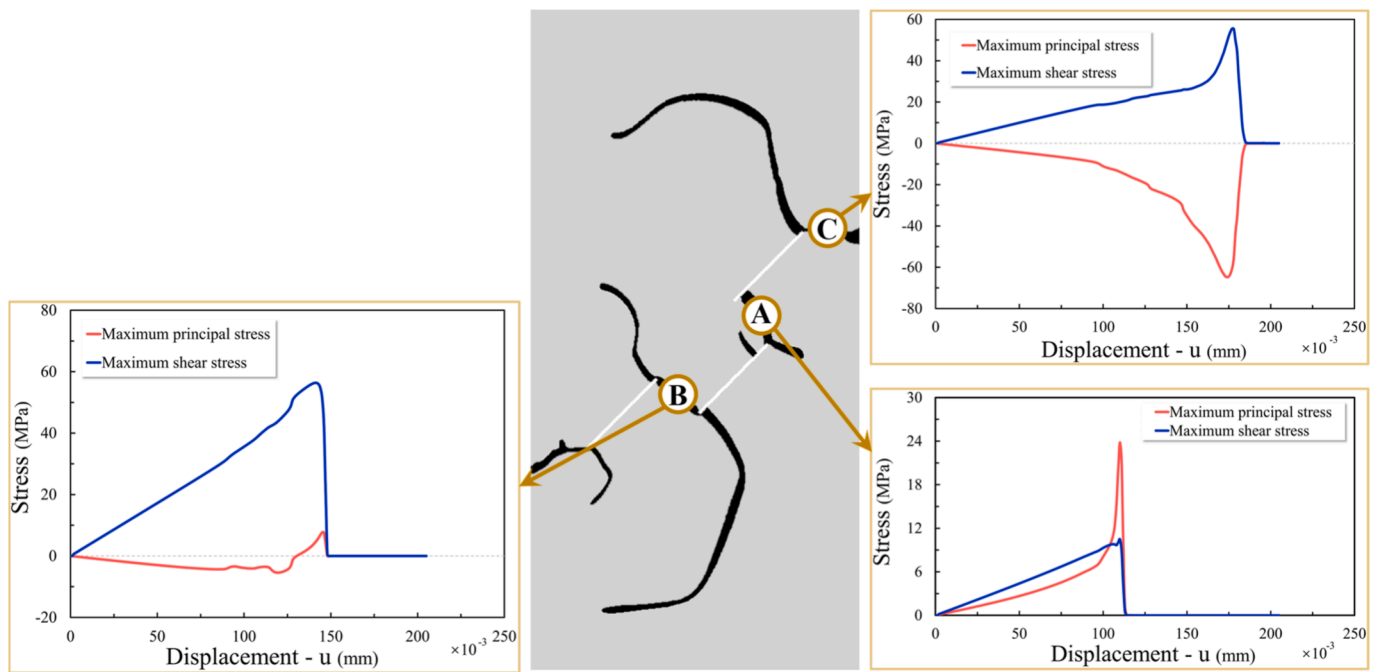


Fig. 32. Maximum principal stress and shear stress as functions of displacement curves at three representative points.

traverses through point C, the stiffness of the point C is compromised, leading to a rapid dissipation of shear stress.

The method proposed showcases predictive capacity for the initiation, growth, merging, and branching of cracks, culminating in the ultimate failure of complex components. Undertaking stress analysis on the test specimen enhances understanding of fracture mechanisms within intricate systems. These attributes herald the proposed method as an up-and-coming numerical tool in engineering applications.

5. Conclusions

In this paper, an improved polygonal numerical scheme for mixed-mode fractures based on the SBFEM and the DPFM was introduced. According to object-oriented programming principles, a flexible SBFEM-DPFM element class, data structure and solving framework are designed and integrated within the self-developed finite element software, GEO-DYNA. Subsequently, the rationality, efficiency, and practicality of the proposed method were demonstrated in different ways through multiple classical examples. Key findings are summarized as follows:

- The proposed method was used to simulate the single-edge notched tensile test, precisely replicating the evolution of fractures and the bearing capacity of the specimen. Furthermore, a uniaxial compression simulation is conducted on a specimen with a 45-degree angle initial crack, illustrating the crack initiation, propagation, branching, and structural progressive failure process. The fracture pattern aligns remarkably well with established research, exhibiting the reliability of the proposed method.
- The study simulated the failure of two uniaxial compression components to evaluate the computational speed improvement achieved through the use of cross-scale mesh and hybrid element methods. The results show that, compared to the global refined mesh approach, the proposed method reduced computation time to just 25 %.
- The intricate mechanisms of fracture nucleation, propagation, and branching that causing failure of the specimen with three 45-degree angle initial cracks under the compression test are discussed. The applicability of complex problems is effectively

demonstrated, and this supplies a reference for studying the service performance of components.

This paper presents a novel approach for analyzing the failure behavior of rock-like materials. While the proposed method still relies on empirical decisions for mesh refinement and adaptation. In future work, we aim to enhance the approach by developing an adaptive meshing strategy and extending it to three-dimensional simulations. These improvements will broaden the method's applicability, increasing its practical utility.

CRediT authorship contribution statement

Yue Zhuo: Writing – review & editing, Writing – original draft, Visualization, Software, Methodology, Conceptualization. **Degao Zou:** Supervision, Software, Funding acquisition. **Kai Chen:** Writing – review & editing, Supervision, Funding acquisition. **Yongqian Qu:** Visualization, Supervision. **Guoyang Yi:** Visualization. **Shanlin Tian:** Visualization.

Declaration of competing interest

The authors declare that they have no known competing financial interests or personal relationships that could have appeared to influence the work reported in this paper.

Acknowledgements

This work was supported by the National Natural Science Foundation of China (Grant Nos. 52192674, 52350393, U2240211).

Data availability

Data will be made available on request.

References

- [1] B. Zp, Speech of Acceptance of the 2009 Timoshenko Medal by Zdeněk P. Bazant, in (2009).

- [2] S.A. Silling, Reformulation of elasticity theory for discontinuities and long-range forces, *J. Mech. Phys. Solids* 48 (2000) 175–209, [https://doi.org/10.1016/S0022-5096\(99\)00029-0](https://doi.org/10.1016/S0022-5096(99)00029-0).
- [3] P. Junker, S. Schwarz, J. Makowski, K. Hackl, A relaxation-based approach to damage modeling, *Contin. Mech. Thermodyn.* 29 (2017) 291–310, <https://doi.org/10.1007/s00161-016-0528-8>.
- [4] X.P. Zhou, J. Bi, Q.H. Qian, Numerical simulation of crack growth and coalescence in rock-like materials containing multiple pre-existing flaws, *Rock Mech. Rock Eng.* 48 (2015) 1097–1114, <https://doi.org/10.1007/s00603-014-0627-4>.
- [5] P.A. Cundall, O.D.L. Strack, A discrete numerical model for granular assemblies, *Geotechnique* 29 (1979) 47–65, <https://doi.org/10.1680/geot.1979.29.1.47>.
- [6] P.A. Cundall, UDEC - A Generalised Distinct Element Program for Modelling Jointed Rock, in: 1980.
- [7] P.A. Cundall, M.P. Board, A Microcomputer program for modelling large-strain plasticity problems. Proceedings of the sixth international conference on numerical methods in geomechanics, 11–15 April 1988, Innsbruck, Austria. Volumes 1 - 3, in, 1988.
- [8] D.O. Potyondy, P.A. Cundall, A bonded-particle model for rock, *Int. J. Rock Mech. Min. Sci.* 41 (2004) 1329–1364, <https://doi.org/10.1016/j.ijrmms.2004.09.011>.
- [9] N. Moës, J. Dolbow, T. Belytschko, A finite element method for crack growth without remeshing, *Int. J. Numer. Meth. Eng.* 46 (1999) 131–150, [https://doi.org/10.1002/\(SICI\)1097-0207\(19990910\)46:1<131::AID-NME726>3.0.CO;2-J](https://doi.org/10.1002/(SICI)1097-0207(19990910)46:1<131::AID-NME726>3.0.CO;2-J).
- [10] M. Eftekhari, A. Baghbanan, H. Hashemolhosseini, Determining stress intensity factor for cracked Brazilian disc using extended finite element method, *Int J Sci Eng Technol* 3 (2014) 890–893, <https://doi.org/10.4028/www.scientific.net/KEM.577-578.285>.
- [11] M. Eftekhari, A. Baghbanan, H. Hashemolhosseini, Extended finite element simulation of crack propagation in cracked Brazilian disc, *Journal of Mining Environ.* 6 (2015) 95–102, <https://doi.org/10.22044/JME.2015.365>.
- [12] M. Eftekhari, A. Baghbanan, H. Hashemolhosseini, Crack propagation in rock specimen under compressive loading using extended finite element method, *Arab. J. Geosci.*, 9 (2016) 145, <https://doi.org/10.1007/s12517-015-2196-6>.
- [13] G.I. Barenblatt, The mathematical theory of equilibrium cracks in brittle fracture, in: H.L. Dryden, T. von Kármán, G. Kuerti, F.H. van den Dungen, L. Howarth (Eds.), *Advances in Applied Mechanics*, Elsevier, 1962, pp. 55–129.
- [14] D.S. Dugdale, Yielding of steel sheets containing slits, *J. Mech. Phys. Solids* 8 (1960) 100–104, [https://doi.org/10.1016/0022-5096\(60\)90013-2](https://doi.org/10.1016/0022-5096(60)90013-2).
- [15] Q. Gong, J. Zhao, A.M. Hefny, Numerical simulation of rock fragmentation process induced by two TBM cutters and cutter spacing optimization, *Tunnelling Underground Space Technology* 21 (2006) 263, <https://doi.org/10.1016/j.tust.2005.12.124>.
- [16] X. Xi, S. Yang, C.I. McDermott, Z.K. Shipton, A. Fraser-Harris, K. Edlmann, Modelling rock fracture induced by hydraulic pulses, *Rock Mech. Rock Eng.* 54 (2021) 3977–3994, <https://doi.org/10.1007/s00603-021-02477-0>.
- [17] P. Liu, Q. Liu, P. Deng, Y. Bo, X. Xie, A novel mixed-mode power exponent cohesive zone model for FDEM and its application to tunnel excavation in the layered rock mass, *Rock Mech. Rock Eng.* 57 (2024) 1219–1243, <https://doi.org/10.1007/s00603-023-03599-3>.
- [18] G.A. Francfort, J.J. Marigo, Revisiting brittle fracture as an energy minimization problem, *J. Mech. Phys. Solids* 46 (1998) 1319–1342, [https://doi.org/10.1016/S0022-5096\(98\)00034-9](https://doi.org/10.1016/S0022-5096(98)00034-9).
- [19] B. Bourdin, G.A. Francfort, J.-J. Marigo, The variational approach to fracture, *J. Elast.* 91 (2008) 5–148, <https://doi.org/10.1007/s10659-007-9107-3>.
- [20] B. Bourdin, G.A. Francfort, J.J. Marigo, Numerical experiments in revisited brittle fracture, *J. Mech. Phys. Solids* 48 (2000) 797–826, [https://doi.org/10.1016/S0022-5096\(99\)00028-9](https://doi.org/10.1016/S0022-5096(99)00028-9).
- [21] C. Miehe, M. Hofacker, F. Welschinger, A phase field model for rate-independent crack propagation: robust algorithmic implementation based on operator splits, *Comput. Meth. Appl. Mech. Eng.*, 199 (2010) 2765–2778, <https://doi.org/10.1016/j.cma.2010.04.011>.
- [22] C. Miehe, F. Welschinger, M. Hofacker, Thermodynamically consistent phase-field models of fracture: variational principles and multi-field FE implementations, *Int. J. Numer. Meth. Eng.* 83 (2010) 1273–1311, <https://doi.org/10.1002/nme.2861>.
- [23] H. Amor, J.-J. Marigo, C. Maurini, Regularized formulation of the variational brittle fracture with unilateral contact: numerical experiments, *J. Mech. Phys. Solids* 57 (2009) 1209–1229, <https://doi.org/10.1016/j.jmps.2009.04.011>.
- [24] M. Ambati, T. Gerasimov, L. De Lorenzis, A review on phase-field models of brittle fracture and a new fast hybrid formulation, *Comput. Mech.* 55 (2015) 383–405, <https://doi.org/10.1007/s00466-014-1109-y>.
- [25] F. Freddi, G. Royer-Carfigni, Variational fracture mechanics to model compressive splitting of masonry-like materials, *Ann. Solid Struct. Mech.* 2 (2011) 57–67, <https://doi.org/10.1007/s12356-011-0018-4>.
- [26] C. McAuliffe, H. Waisman, A unified model for metal failure capturing shear banding and fracture, *Int. J. Plast.* 65 (2015) 131–151.
- [27] C. McAuliffe, H. Waisman, A coupled phase field shear band model for ductile–brittle transition in notched plate impacts, *Comput. Methods Appl. Mech. Eng.* 305 (2016) 173–195.
- [28] Z. Khalil, A.Y. Elghazouli, E. Martínez-Pañeda, A generalised phase field model for fatigue crack growth in elastic–plastic solids with an efficient monolithic solver, *Comput. Methods Appl. Mech. Eng.*, 388 (2022) 114286, <https://doi.org/10.1016/j.cma.2021.114286>.
- [29] E.C. Bryant, W. Sun, A mixed-mode phase field fracture model in anisotropic rocks with consistent kinematics, *Comput. Meth. Appl. Mech. Eng.*, 342 (2018) 561–584, <https://doi.org/10.1016/j.cma.2018.08.008>.
- [30] F. Fei, J. Choo, Double-phase-field formulation for mixed-mode fracture in rocks, *Comput. Meth. Appl. Mech. Eng.*, 376 (2021) 113655, <https://doi.org/10.1016/j.cma.2020.113655>.
- [31] S. Liu, Y. Wang, C. Peng, W. Wu, A thermodynamically consistent phase field model for mixed-mode fracture in rock-like materials, *Comput. Meth. Appl. Mech. Eng.*, 392 (2022) 114642, <https://doi.org/10.1016/j.cma.2022.114642>.
- [32] Y.-S. Lo, T.J.R. Hughes, C.M. Landis, Phase-field fracture modeling for large structures, *J. Mech. Phys. Solids* 171 (2023) 105118, <https://doi.org/10.1016/j.jmps.2022.105118>.
- [33] J.-Y. Wu, Y. Huang, H. Zhou, V.P. Nguyen, Three-dimensional phase-field modeling of mode I+ II/III failure in solids, *Comput. Methods Appl. Mech. Eng.* 373 (2021) 113537, <https://doi.org/10.1016/j.cma.2020.113537>.
- [34] T. You, Q.-Z. Zhu, P.-F. Li, J.-F. Shao, Incorporation of tension-compression asymmetry into plastic damage phase-field modeling of quasi brittle geomaterials, *Int. J. Plast.* 124 (2020) 71–95, <https://doi.org/10.1016/j.ijplas.2019.08.003>.
- [35] Z. Yu, Y. Sun, M.-N. Vu, J.-F. Shao, Modeling of mixed cracks in rock-like brittle materials under compressive stresses by a double-phase-field method, *Rock Mech. Rock Eng.* 56 (2023) 2779–2792, <https://doi.org/10.1007/s00603-022-03196-w>.
- [36] X. Zhang, S.W. Sloan, C. Vignes, D. Sheng, A modification of the phase-field model for mixed mode crack propagation in rock-like materials, *Comput. Methods Appl. Mech. Eng.* 322 (2017) 123–136, <https://doi.org/10.1016/j.cma.2017.04.028>.
- [37] S. Zhou, X. Zhuang, T. Rabczuk, Phase field modeling of brittle compressive-shear fractures in rock-like materials: a new driving force and a hybrid formulation, *Comput. Methods Appl. Mech. Eng.* 355 (2019) 729–752, <https://doi.org/10.1016/j.cma.2019.06.021>.
- [38] S. Zhou, X. Zhuang, H. Zhu, T. Rabczuk, Phase field modelling of crack propagation, branching and coalescence in rocks, *Theor. Appl. Fract. Mech.* 96 (2018) 174–192, <https://doi.org/10.1016/j.tafmec.2018.04.011>.
- [39] Y. Xu, S. Zhou, C. Xia, Y. Hu, A new phase field model for mixed-mode brittle fractures in rocks modified from triple shear energy criterion, *Acta Geotech. Applied Mathematical Modelling* 17 (2022) 5613–5637, <https://doi.org/10.1007/s11440-022-01589-3>.
- [40] L. Greco, A. Patton, M. Negri, A. Marengo, U. Perego, A. Reali, Higher order phase-field modeling of brittle fracture via isogeometric analysis, *Eng. Comput.* (2024), <https://doi.org/10.1007/s00366-024-01949-5>.
- [41] Hirshikesh, A.L.N. Pramod, R.K. Annabattula, E.T. Ooi, C. Song, S. Natarajan, Adaptive phase-field modeling of brittle fracture using the scaled boundary finite element method, *Comput. Methods Appl. Mech. Eng.* 355 (2019) 284–307, <https://doi.org/10.1016/j.cma.2019.06.002>.
- [42] J.-Y. Wu, V.P. Nguyen, C.T. Nguyen, D. Sutula, S. Sinaie, S.P.A. Bordas, Chapter One - Phase-field modeling of fracture, in: S.P.A. Bordas, D.S. Balint (Eds.), *Advances in applied mechanics*, Elsevier, 2020, pp. 1–183, <https://doi.org/10.1016/b.s.aams.2019.08.001>.
- [43] G. Zhang, C. Tang, P. Chen, G. Long, J. Cao, S. Tang, Advancements in phase-field modeling for fracture in nonlinear elastic solids under finite deformations, *Mathematics* 11 (2023) 3366, <https://doi.org/10.3390/math11153366>.
- [44] D.J. Rixen, Extended preconditioners for the FETI method applied to constrained problems, *Int. J. Numer. Meth. Eng.* 54 (2002) 1–26, <https://doi.org/10.1002/nme.412>.
- [45] H. Bavestrello, P. Avery, C. Farhat, Incorporation of linear multipoint constraints in domain-decomposition-based iterative solvers – Part II: blending FETI-DP and mortar methods and assembling floating substructures, *Comput. Methods Appl. Mech. Eng.*, 196 (2007) 1347–1368, <https://doi.org/10.1016/j.cma.2006.03.024>.
- [46] J.-G. Ahn, H. Yang, J.G. Kim, Multipoint constraints with lagrange multiplier for system dynamics and its reduced-order modeling, *AIAA J.* 58 (2020) 385–401, <https://doi.org/10.2514/1.J058118>.
- [47] E.L. Wachspress, S.M. Rohde, A Rational Finite Element Basis, in, 1975.
- [48] M.S. Floater, Mean value coordinates, *Comput. Aided Geom. Des.* 20 (2003) 19–27, [https://doi.org/10.1016/S0167-8396\(03\)00002-5](https://doi.org/10.1016/S0167-8396(03)00002-5).
- [49] A. Tabarraei, N. Sukumar, Adaptive computations on conforming quadtree meshes, *Finite Elem. Anal. Des.* 41 (2005) 686–702, <https://doi.org/10.1016/j.finel.2004.08.002>.
- [50] C. Song, J.P. Wolf, The scaled boundary finite-element method—alias consistent infinitesimal finite-element cell method—for elastodynamics, *Comput. Methods Appl. Mech. Eng.* 147 (1997) 329–355, [https://doi.org/10.1016/S0045-7825\(97\)00021-2](https://doi.org/10.1016/S0045-7825(97)00021-2).
- [51] C. Song, J.P. Wolf, The scaled boundary finite-element method: analytical solution in frequency domain, *Comput. Methods Appl. Mech. Eng.* 164 (1998) 249–264, [https://doi.org/10.1016/S0045-7825\(98\)00058-9](https://doi.org/10.1016/S0045-7825(98)00058-9).
- [52] C. Song, J.P. Wolf, Body loads in scaled boundary finite-element method, *Comput. Methods Appl. Mech. Eng.* 180 (1999) 117–135, [https://doi.org/10.1016/S0045-7825\(99\)00052-3](https://doi.org/10.1016/S0045-7825(99)00052-3).
- [53] C. Song, J.P. Wolf, The scaled boundary finite-element method—a primer: solution procedures, *Comput. Struct.* 78 (2000) 211–225.
- [54] J.P. Wolf, C. Song, The scaled boundary finite-element method—a primer: derivations, *Comput. Struct.* 78 (2000) 191–210.
- [55] A.J. Deeks, J.P. Wolf, A virtual work derivation of the scaled boundary finite-element method for elastostatics, *Comput. Mech.* 28 (2002) 489–504.

- [56] K. Chen, D. Zou, X. Kong, J. Liu, Elasto-plastic fine-scale damage failure analysis of metro structures based on coupled SBFEM-FEM, *Comput. Geotech.* 108 (2019) 280–294, <https://doi.org/10.1016/j.compgeo.2018.12.030>.
- [57] W. Ye, J. Liu, H. Fang, G. Lin, High-performance analysis of the interaction between plate and multi-layered elastic foundation using SBFEM-FEM, *Compos. Struct.* 214 (2019) 1–11, <https://doi.org/10.1016/j.compstruct.2019.01.104>.
- [58] M. Zhao, P. Liu, J. Zhang, G. Zhang, Z. Gao, X. Du, A direct time-domain FEM-SBFEM-SBPML method for soil-structure interaction analysis using quadtree mesh, *Comput. Geotech.* 161 (2023) 105597, <https://doi.org/10.1016/j.compgeo.2023.105597>.
- [59] G. Zhang, M. Zhao, X. Du, J. Zhang, Time-domain scaled boundary perfectly matched layer for elastic wave propagation, *Int. J. Numer. Meth. Eng.* 124 (2023) 3906–3934, <https://doi.org/10.1002/nme.7300>.
- [60] J. Zhang, P. Wang, M. Zhao, L. Liu, Y.-C. Qu, X.-L. Du, A scaled boundary finite element method for soil dynamic impedance of pile groups using hybrid quadtree mesh considering horizontal vibration, *Eng. Anal. Bound. Elem.* (2023), <https://doi.org/10.1016/jenganabound.2023.05.029>.
- [61] G. Zhang, M. Zhao, J. Zhang, J. Wang, X. Du, Scaled boundary perfectly matched layer for wave propagation in a three-dimensional poroelastic medium, *App. Math. Model.* 125 (2024) 108–138, <https://doi.org/10.1016/j.apm.2023.09.028>.
- [62] J. Liu, W.-Q. Zhang, W.-B. Ye, L. Gan, L. Qin, Q.-S. Zang, H.-B. Wang, Forced vibration of liquid-filled composite laminated shell container considering fluid-structure interaction by the scaled boundary finite element method, *Phys. Fluids* 36 (2024), <https://doi.org/10.1063/5.0221695>.
- [63] J. Liu, C. Hao, Y. Zhou, W. Ye, Dynamic analysis of functionally graded sandwich beams using a semi-analytic method named scaled boundary finite element method, *Eng. Anal. Bound. Elem.* 130 (2021) 161–175, <https://doi.org/10.1016/jenganabound.2021.05.010>.
- [64] S. Jiang, C. Du, Study on dynamic interaction between crack and inclusion or void by using XFEM, *Struct. Eng. Mech.* 63 (2017) 329–345, <https://doi.org/10.12989/sem.2017.63.3.329>.
- [65] N. Xiupeng, K. Chen, D. Zou, X. Kong, J. Liu, Y. Qu, Slope stability analysis based on SBFEM and multistage polytree-based refinement algorithms, *Comput. Geotech.* 149 (2022) 104861, <https://doi.org/10.1016/j.compgeo.2022.104861>.
- [66] A. Yaseri, M.H. Bazayr, N. Hataf, 3D coupled scaled boundary finite-element/finite-element analysis of ground vibrations induced by underground train movement, *Comput. Geotech.* 60 (2014) 1–8, <https://doi.org/10.1016/j.compgeo.2014.03.013>.
- [67] A. Yaseri, M.H. Bazayr, S. Javady, 2.5 D coupled FEM-SBFEM analysis of ground vibrations induced by train movement, *Soil Dyn. Earthq. Eng.* 104 (2018) 307–318, <https://doi.org/10.1016/j.soildyn.2017.10.021>.
- [68] A. Yaseri, J.-M. Konrad, Computation of amplification functions of earth dam-flexible canyon systems by the hybrid FEM-SBFEM technique, *Earthq. Eng. Struct. Dyn.* 50 (2021) 2883–2896, <https://doi.org/10.1002/eqe.3477>.
- [69] H. Chen, S. Natarajan, E.T. Ooi, C. Song, Modeling of coupled thermo-mechanical crack propagation in brittle solids using adaptive phase field method with scaled boundary finite element method, *Theor. Appl. Fract. Mech.* 129 (2024), <https://doi.org/10.1016/j.tafmec.2023.104158>.
- [70] D.R. Wijesinghe, S. Natarajan, G. You, M. Khandelwal, A. Dyson, C. Song, E. T. Ooi, Adaptive phase-field modelling of fracture propagation in poroelastic media using the scaled boundary finite element method, *Comput. Methods Appl. Mech. Eng.* 411 (2023), <https://doi.org/10.1016/j.cma.2023.116056>.
- [71] S. Natarajan, E.T. Ooi, C. Birk, C. Song, Adaptive modelling of dynamic brittle fracture - a combined phase field regularized cohesive zone model and scaled boundary finite element approach, *Int. J. Fract.* 236 (2022) 87–108, <https://doi.org/10.1007/s10704-022-00634-2>.
- [72] R. Assaf, C. Birk, S. Natarajan, H. Gravenkamp, Three-dimensional phase-field modeling of brittle fracture using an adaptive octree-based scaled boundary finite element approach, *Comput. Methods Appl. Mech. Eng.* 399 (2022), <https://doi.org/10.1016/j.cma.2022.115364>.
- [73] A.L.N. Pramod, S. Natarajan, E.T. Ooi, Application of adaptive phase-field scaled boundary finite element method for functionally graded materials, *Int. J. Comput. Methods* 18 (2021), <https://doi.org/10.1142/S0219876220410078>.
- [74] Y. Zhuo, D. Zou, K. Chen, J. Liu, Y. Qu, G. Yi, A coupled scaled boundary finite element and phase-field algorithm for seismic loading, *Eng. Anal. Bound. Elem.* 169 (2024) 106009, <https://doi.org/10.1016/jenganabound.2024.106009>.
- [75] K. Yu, Z. Yang, H. Li, E. Tat Ooi, S. Li, G. Liu, A mesoscale modelling approach coupling SBFEM, continuous damage phase-field model and discrete cohesive crack model for concrete fracture, *Eng. Fract. Mech.* 278 (2023), <https://doi.org/10.1016/j.engfractmech.2022.109030>.
- [76] P. Zhang, K. Douglas, H. Chen, C. Song, A.R. Russell, Non-dimensionalization and scaling of fracture processes in concrete and rock, *Eng. Fract. Mech.* 297 (2024) 109854, <https://doi.org/10.1016/j.engfractmech.2024.109854>.
- [77] C. Song, A matrix function solution for the scaled boundary finite-element equation in statics, *Comput. Methods Appl. Mech. Eng.* 193 (2004) 2325–2356, <https://doi.org/10.1016/j.cma.2004.01.017>.
- [78] E.T. Ooi, C. Song, F. Tin-Loi, A scaled boundary polygon formulation for elastoplastic analyses, *Comput. Methods Appl. Mech. Eng.* 268 (2014) 905–937, <https://doi.org/10.1016/j.cma.2013.10.021>.
- [79] K. Chen, D. Zou, X. Kong, A. Chan, Z. Hu, A novel nonlinear solution for the polygon scaled boundary finite element method and its application to geotechnical structures, *Comput. Geotech.* 82 (2017) 201–210, <https://doi.org/10.1016/j.compgeo.2016.09.013>.
- [80] K.X. Zou D, Liu J et al., Theoretical Introduction and User Manual of the GEODYNA7.0 : A High-Performance Finite Element Analysis Software System for Large-Scale Geotechnical Engineering, Institute of earthquake engineering, Dalian University of Technology ed., Dalian, 2022.
- [81] K. Chen, D. Zou, X. Kong, X. Yu, An efficient nonlinear octree SBFEM and its application to complicated geotechnical structures, *Comput. Geotech.* 96 (2018) 226–245, <https://doi.org/10.1016/j.compgeo.2017.10.021>.
- [82] K. Chen, D. Zou, X. Kong, Y. Zhou, Global concurrent cross-scale nonlinear analysis approach of complex CFRD systems considering dynamic impervious panel-rockfill material-foundation interactions, *Soil Dyn. Earthq. Eng.* 114 (2018) 51–68, <https://doi.org/10.1016/j.soildyn.2018.06.027>.
- [83] K. Chen, D. Zou, J. Liu, Y. Zhuo, A high-precision formula for mixed-order polygon elements based on SBFEM, *Comput. Geotech.* 155 (2023) 105209, <https://doi.org/10.1016/j.compgeo.2022.105209>.
- [84] K. Chen, D. Zou, H. Tang, J. Liu, Y. Zhuo, Scaled boundary polygon formula for Cosserat continuum and its verification, *Eng. Anal. Bound. Elem.* 126 (2021) 136–150, <https://doi.org/10.1016/jenganabound.2021.02.007>.
- [85] J. Gong, D. Zou, X. Kong, J. Liu, K. Chen, A coupled meshless-SBFEM-FEM approach in simulating soil-structure interaction with cross-scale model, *Soil Dyn. Earthq. Eng.* 136 (2020) 106214, <https://doi.org/10.1016/j.soildyn.2020.106214>.
- [86] J. Gong, D. Zou, X. Kong, J. Liu, K. Chen, The simulation of high compressive stress and extrusion phenomenon for concrete face slabs in CFRDs under strong seismic loads, *Soil Dyn. Earthq. Eng.* 147 (2021) 106792, <https://doi.org/10.1016/j.soildyn.2021.106792>.
- [87] J. Gong, D. Zou, X. Kong, J. Liu, Y. Qu, An approach for simulating the interaction between soil and discontinuous structure with mixed interpolation interface, *Eng. Struct.* 237 (2021) 112035, <https://doi.org/10.1016/j.engstruct.2021.112035>.
- [88] J. Gong, D. Zou, X. Kong, Y. Qu, J. Liu, An extended meshless method for 3D interface simulating soil-structure interaction with flexibly distributed nodes, *Soil Dyn. Earthq. Eng.* 125 (2019) 105688, <https://doi.org/10.1016/j.soildyn.2019.05.027>.
- [89] L. Jingmao, Z. Degao, N. Fanwei, K. Xianjing, A unified constitutive model for instantaneous elastic-plastic and time-dependent creep behaviour of gravelly soils under complex loading, *Can. Geotech. J.* (2023), <https://doi.org/10.1139/cgj-2022-0635>.
- [90] J. Liu, D. Zou, X. Kong, A two-mechanism soil-structure interface model for three-dimensional cyclic loading, *Int. J. Numer. Anal. Meth. Geomech.* 44 (2020) 2042–2069, <https://doi.org/10.1002/nag.3118>.
- [91] F. Ning, J. Liu, X. Kong, D. Zou, Critical state and grading evolution of rockfill material under different triaxial compression tests, *Int. J. Geomech.* 20 (2020) 04019154, [https://doi.org/10.1061/\(ASCE\)GM.1943-5622.0001550](https://doi.org/10.1061/(ASCE)GM.1943-5622.0001550).
- [92] Y. Qu, D. Zou, K. Chen, J. Liu, Three-dimensional refined analysis of seismic cracking and anti-seismic measures performance of concrete face slab in CFRDs, *Comput. Geotech.* 139 (2021) 104376, <https://doi.org/10.1016/j.compgeo.2021.104376>.
- [93] Y. Qu, D. Zou, X. Kong, J. Liu, Y. Zhang, X. Yu, Seismic damage performance of the steel fiber reinforced face slab in the concrete-faced rockfill dam, *Soil Dyn. Earthq. Eng.* 119 (2019) 320–330, <https://doi.org/10.1016/j.soildyn.2019.01.018>.
- [94] Y. Qu, D. Zou, X. Kong, X. Yu, K. Chen, Seismic cracking evolution for anti-seepage face slabs in concrete faced rockfill dams based on cohesive zone model in explicit SBFEM-FEM frame, *Soil Dyn. Earthq. Eng.* 133 (2020) 106106, <https://doi.org/10.1016/j.soildyn.2020.106106>.
- [95] Y. Qu, D. Zou, J. Liu, Z. Yang, K. Chen, Two-dimensional DEM-FEM coupling analysis of seismic failure and anti-seismic measures for concrete faced rockfill dam, *Comput. Geotech.* 151 (2022) 104950, <https://doi.org/10.1016/j.compgeo.2022.104950>.
- [96] J.-Y. Wu, Y. Huang, V.P. Nguyen, On the BFGS monolithic algorithm for the unified phase field damage theory, *Comput. Methods Appl. Mech. Eng.*, 360 (2020) 112704, <https://doi.org/10.1016/j.cma.2019.112704>.
- [97] G. Molnár, A. Gravouil, 2D and 3D Abaqus implementation of a robust staggered phase-field solution for modeling brittle fracture, *Finite Elem. Anal. Des.* 130 (2017) 27–38, <https://doi.org/10.1016/j.finel.2017.03.002>.
- [98] M.L. Benzeggagh, M. Kenane, Measurement of mixed-mode delamination fracture toughness of unidirectional glass/epoxy composites with mixed-mode bending apparatus, *Compos. Sci. Technol.* 56 (1996) 439–449, [https://doi.org/10.1016/0266-3538\(96\)00005-X](https://doi.org/10.1016/0266-3538(96)00005-X).
- [99] Y. Cao, W. Wang, W. Shen, X. Cui, J. Shao, A new hybrid phase-field model for modeling mixed-mode cracking process in anisotropic plastic rock-like materials, *Int. J. Plast.* 157 (2022) 103395, <https://doi.org/10.1016/j.ijplas.2022.103395>.
- [100] Z. Cheng, D. Dias-da-Costa, Y. Gan, L. Shen, A modified phase-field model for predicting mixed-mode fracture in rock-like materials, *Journal of Micromechanics and Molecular Physics* 07 (2022), <https://doi.org/10.1142/S2424913022410065>.
- [101] Y. Hou, P. Yue, Q. Xin, T. Pauli, W. Sun, L. Wang, Fracture failure of asphalt binder in mixed mode (Modes I and II) by using phase-field model, *Road Mater. Pavement Des.* 15 (2014) 167–181, <https://doi.org/10.1080/14680629.2013.866155>.
- [102] L. Hug, M. Potten, G. Stockinger, K. Thuro, S. Kollmannsberger, A three-field phase-field model for mixed-mode fracture in rock based on experimental determination of the mode II fracture toughness, *Eng. Comput.* 38 (2022) 5563–5581, <https://doi.org/10.1007/s00366-022-01684-9>.
- [103] Z.-M. Jia, X.-P. Zhou, F. Berto, Compressive-shear fracture model of the phase-field method coupled with a modified Hoek-Brown criterion, *Int. J. Fract.* 229 (2021) 161–184, <https://doi.org/10.1007/s10704-021-00546-7>.

- [104] Q. Rao, C. Zhao, W. Yi, A new mixed-mode phase-field model for crack propagation of brittle rock, *J. Rock Mech. Geotech. Eng.* 15 (2023) 1186–1199, <https://doi.org/10.1016/j.jrmge.2022.10.019>.
- [105] B.-T. Shen, O. Stephansson, Modification of the G-criterion for crack propagation subjected to compression, *Eng. Fract. Mech.* 47 (1994) 177–189, [https://doi.org/10.1016/0013-7944\(94\)90219-4](https://doi.org/10.1016/0013-7944(94)90219-4).
- [106] A. Spetz, R. Denzer, E. Tudisco, O. Dahlblom, A Modified Phase-Field Fracture Model for Simulation of Mixed Mode Brittle Fractures and Compressive Cracks in Porous Rock, *Rock Mech. Rock Eng.* 54 (2021) 5375–5388, <https://doi.org/10.1007/s00603-021-02627-4>.
- [107] F. Zhu, H. Tang, D. Zhou, Y. Li, An efficient adaptive multi-mesh phase-field method for simulating rock fractures, *Comput. Geotech.* 163 (2023) 105765, <https://doi.org/10.1016/j.compgeo.2023.105765>.
- [108] H. Zhu, Q. Wang, X. Zhuang, A nonlinear semi-concurrent multiscale method for fractures, *Int. J. Impact Eng.* 87 (2016) 65–82, <https://doi.org/10.1016/j.ijimpeng.2015.06.022>.
- [109] M. Hu, Q. Tan, D. Feng, Y. Ren, Y. Huang, Simulation of rock crack propagation and failure behavior based on a mixed failure model with SPH, *Rock Mech. Rock Eng.* (2024), <https://doi.org/10.1007/s00603-024-04001-6>.
- [110] Q. Yin, H. Jing, H. Su, Investigation on mechanical behavior and crack coalescence of sandstone specimens containing fissure-hole combined flaws under uniaxial compression, *Geosci. J.* 22 (2018) 825–842, <https://doi.org/10.1007/s12303-017-0081-x>.